minerals

MDPI

Article

Geological Constraints on the Genesis of Jagpura Au-Cu Deposit NW India: Implications from Magnetite-Apatite Mineral Chemistry, Fluid Inclusion and Sulfur Isotope Study

Abhishek Anand [1,2], Sahendra Singh [2,*], Arindam Gantait [1], Amit Srivastava [1], Girish Kumar Mayachar [3] and Manoj Kumar [4]

[1] State Unit Rajasthan, Geological Survey of India, Western Region, Jaipur 302004, India
[2] Department of Applied Geology, Indian Institute of Technology (ISM), Dhanbad 826004, India
[3] Geological Survey of India, NCEGR, Bengaluru 560078, India
[4] State Unit Madhya Pradesh, Geological Survey of India, Central Region, Bhopal 462016, India
* Correspondence: sahendra@iitism.ac.in

Abstract: The Jagpura Au-Cu deposit is situated within the Aravalli craton in the northwestern part of India. In the present work, petrography, mineral chemistry, fluid inclusion and sulfur isotopic compositions were used to study the Jagpura Au-Cu deposit. The ore mineral association of the deposit is arsenopyrite, loellingite, chalcopyrite, pyrrhotite and pyrite, along with native gold, magnetite and apatite. The gold fineness ranges from 914–937‰ (avg. 927‰). The presence of Au-Bi-Te phases, pyrite (>1 Co/Ni ratio), magnetite (≥1 Ni/Cr ratio, <1 Co/Ni ratio) and apatite (>1 F/Cl ratio) suggest the hydrothermal origin Au-Cu mineralization. A fluid inclusion study indicates the different episodes of fluid immiscibility with the homogenization temperatures varying between 120–258 °C and salinities range within the 8.86–28.15 wt% NaCl eq. The sulfur isotopic composition of sulfides varies from 8.98 to 14.58‰ (avg. 11.16‰). It is inferred that the variation in the sulfur isotopic compositions of sulfides is due to the cooling and dilution of the metalliferous fluid of mixed origin, derived from the basement meta-sedimentary rocks and the high saline basinal fluid. The iron oxide-copper-gold-apatite associations, structural control of mineralization, pervasive hydrothermal alteration, fluid salinity and sulfur isotope compositions indicate that the Jagpura Au-Cu deposit is similar to the iron oxide-copper-gold (IOCG)-iron oxide-apatite (IOA)types of deposits. Based on the ore geochemistry and the trace elements systematic of magnetite, the deposit is further classified as an IOCG-IOA type: IOCG-Co (reduced) subtype.

Keywords: Jagpura Au-Cu deposit; Aravalli Craton; high fineness gold; hydrothermal magnetite; fluid inclusions; sulfur isotopic composition; IOCG-IOA type: IOCG-Co (reduced) subtype mineralization

Citation: Anand, A.; Singh, S.; Gantait, A.; Srivastava, A.; Mayachar, G.K.; Kumar, M. Geological Constraints on the Genesis of Jagpura Au-Cu Deposit NW India: Implications from Magnetite-Apatite Mineral Chemistry, Fluid Inclusion and Sulfur Isotope Study. *Minerals* **2022**, *12*, 1345. https://doi.org/10.3390/min12111345

Academic Editor: Galina Palyanova

Received: 27 September 2022
Accepted: 19 October 2022
Published: 24 October 2022

1. Introduction

Gold occurs mainly in a native state and often contains Ag, Cu, Hg and other impurities [1,2]. Native gold is an indicator mineral of gold deposits [2,3]. On the basis of their genesis, the gold deposits are classified into different types, viz. Orogenic lode gold, Carlin-type gold deposit, Porphyry type gold and Iron oxide-copper-gold (IOCG) type gold deposit [4–10]. The majority of these gold deposits is of hydrothermal origin and constitute a significant portion of the world's gold resources [11].In these deposits, gold mineralization is commonly associated with pyrite and magnetite. Magnetite is stable across a wide variety of physicochemical circumstances and contains various trace elements, including Al, Ti, Mg, Mn, Zn, Cr, V, Ni, Co, and Ga [12–16]. These elements are useful petrogenetic tools for modern-day exploration [15,17–22]. Accordingly, magnetite's trace element composition is used to distinguish between IOCG, Volcanogenic Massive Sulfide

(VMS), copper porphyry, Cu-Fe skarn, magmatic Fe-Ti-V-Cr, Ni-Cu-PGE, Kiruna-type iron oxide-apatite (IOA) and BIF deposits [14,16,18,20,22–28]. Apatite is also a vital pathfinder mineral for IOCG/IOCG-IOA type deposits and is effectively used as an indicator mineral for IOCG system [29,30].

The Jagpura Au-Cu deposit lies in the southern part of the Salumber-Ghatol Metallogenic Belt (SGMB), within the Paleoproterozoic Aravali Delhi Fold Belt (ADFB) Rajasthan, India. The Au-Cu mineralization of the SGMB, is hosted by carbonate rocks and albitite [27,31,32]. Previous workers advocated the magmatic-hydrothermal model for the origin of gold-sulfide mineralization within the Bhukia-Jagpura deposit [33]. However, recent investigations in the Jagpura deposit reveals that the Au-Cu lodes are hosted within the albitite and quartz-mica schist [34,35]. Since, the Jagpura Au-Cu deposit is a relatively recent finding; there are significant gaps in the understanding of the nature of the gold-sulfide mineralization, associated magnetite-apatite mineral chemistry, and source-transportation-precipitation mechanism of the ore bearing fluid to form the deposit. This requires a detailed investigation of the mineralization and hence, an integrated approach is attempted to constrain the genesis of gold-copper mineralization.

The present study was carried out with an aim to (i) characterize the gold mineralization associated with magnetite and apatite, (ii) understand the possible source of ore-bearing fluids and (iii) classify the Jagpura deposit in the light of the recent classification scheme for Cu-Au-Fe (CGI)/ IOCG deposits [36]. In this work, we present new data on the genetic aspects incorporating mineral chemistry of Au, Au-Bi, Bi-Te, Cu-sulfide phases, besides associated magnetite and apatite, the sulfur isotopic composition of major ore minerals, and fluid inclusion micro-thermometry of mineralized quartz veins of the Jagpura deposit. This study fills up the existing gaps in the understanding of the metallogeny of the Salumber-Ghatol Metallogenic Belt and has a broader exploration implication on this belt and allied areas of similar geological settings.

2. Regional Geological Setting

The Northwestern Indian shield is represented by 3.3–2.5 Ga Archean basement known as the Banded Gneissic Complex (BGC) and is overlain by 2.2–1.85 Ga Paleoproterozoic cover sequence of Aravalli-Delhi Fold Belt (ADFB), (Figure 1), [37–41]. The Archean basement consists of granite gneiss with meta-volcano-sedimentary rocks and intrusive rocks [38,39]. The BGC is in tectonic contact with or unconformably overlain by two Proterozoic supracrustal sequences, the Aravalli and Delhi supergroups [42]. The Aravalli Supergroup is widely distributed in the eastern and southeastern parts of the Aravalli-Delhi Fold Belt. The relationship between ADFB and BGC is unconformable along the entire Aravalli Fold Belt margin [42].

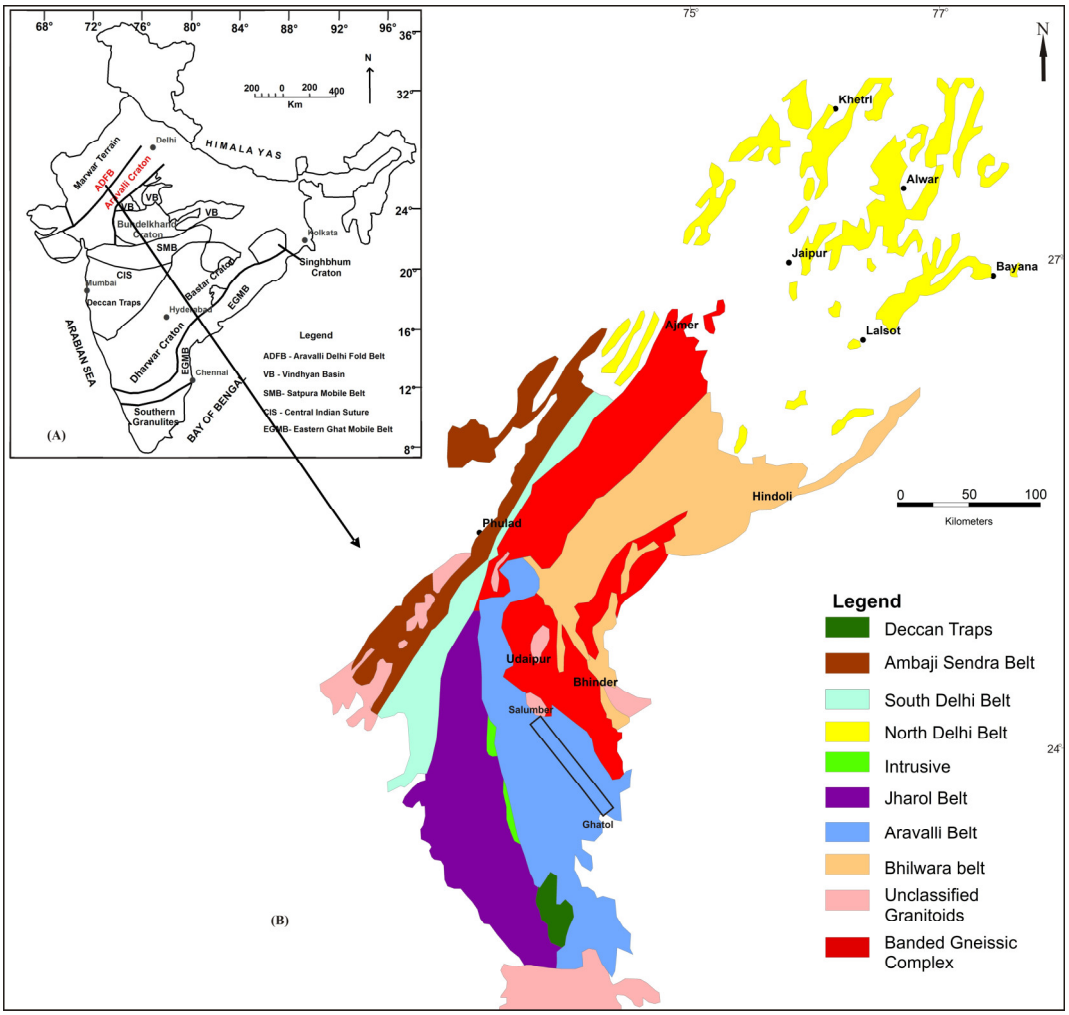

Figure 1. (**A**) Inset map showing the location of the Aravalli craton and Aravalli Delhi Fold Belt in Indian subcontinent, modified from reference [43]; (**B**) Geological map of the Aravalli–Delhi Fold Belt showing location of the basement Banded Gneissic Complex (BGC), Paleoproterozoic Aravalli Supergroup and Salumber-Ghatol metallogenic belt, modified from references [44].

The ADFB is composed of calcareous and argillaceous meta-sedimentary rocks, meta-volcano-sedimentary rocks, and intrusive rocks. The Aravalli sequence belongs to the continental rift basin settings [45,46]. Geochronological studies showed that the Aravalli sedimentation period ranges from ~2.3 to ~1.6 Ga [47,48]. The 4–6 km wide and 70 km long Salumber-Ghatol Metallogenic Belt (SGMB) is exposed in the extreme southeastern part of the ADFB and forms a part of the eastern margin of the Debari Group of the Aravalli Supergroup. It extends from Salumber in the northwest to Ghatol in the southeast, exposing a meta-volcano-sedimentary sequence unconformably overlying the BGC (Figure 2), [49,50]. Staurolite schist is a part of the basement rock [51]. The contact between the staurolite schist of the BGC and the meta-sediments of the Jagpura Formation of the Debari Group is sheared and referred to as Ghatol Shear Zone [31]. The lithostratigraphic sequence of the Debari Group, exposed in the SGMB is classified into five formations viz., the Gurali Formation (Basal quartzite and conglomerate), Delwara Formation (metabasalt with intercalations of conglomerate, marble, quartzite and feldspathic schist), Jaisamand Formation (conglomerate, feldspathic quartzite, mica schist and dolomitic marble), Mukandpura Formation (dolomite, phyllite and carbonaceous phyllite with intercalations of mica schist) and Jagpura Formation (quartzite, quartz-mica schist, garnet-biotite schist, dolomitic marble, calc-silicate rock and amphibolite).

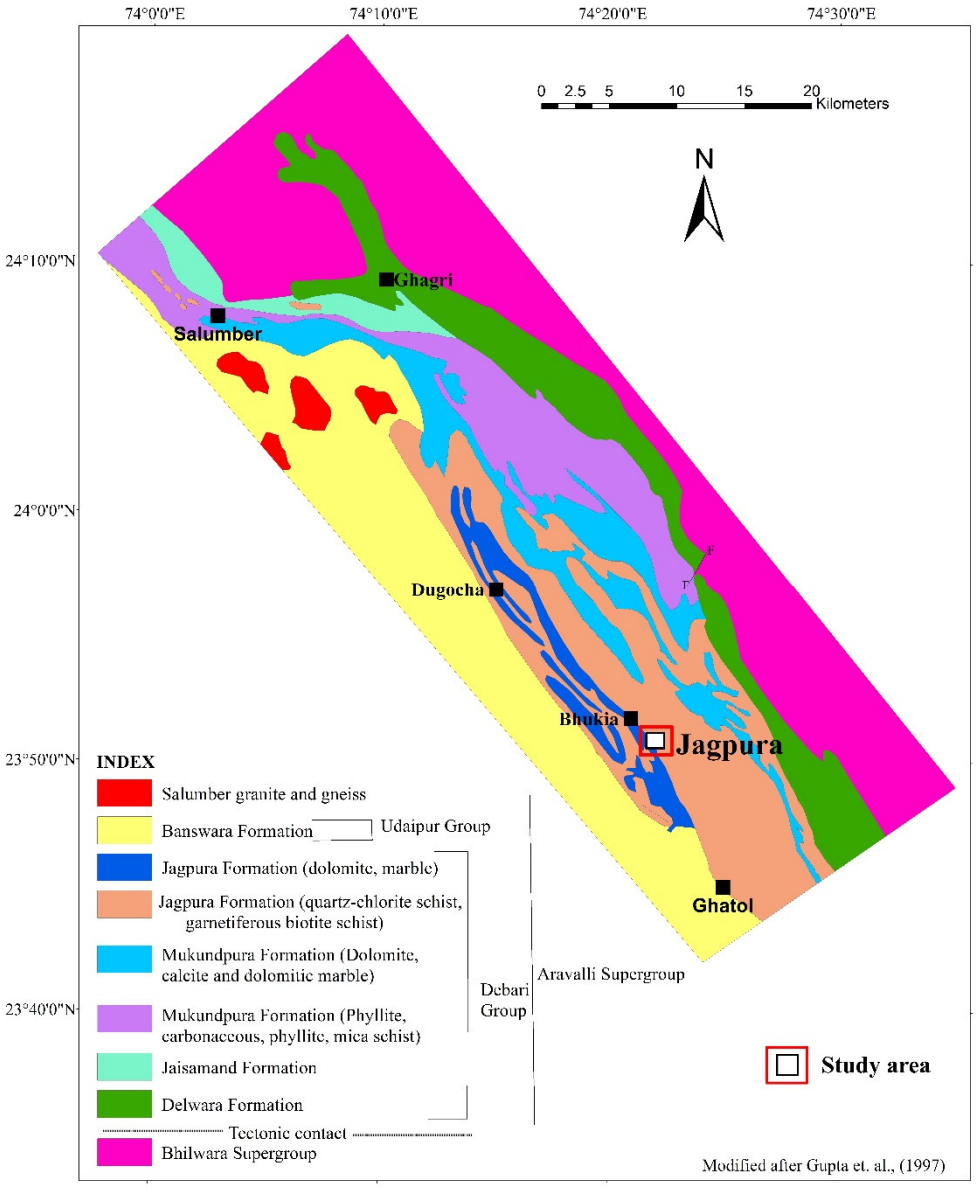

Figure 2. Geological map of Salumber-Ghatol metallogenic belt showing location of study area, modified from reference [51].

The general structural trend of the lithologic units of the SGMB is NNW-SSE with moderate to steep dips towards WSW. The rocks of the SGMB are affected by three phases of deformation events [33,52] and have undergone upper greenschist to middle amphibolite facies metamorphism [53]. The lower part of the Aravalli Supergroup i.e., Debari Group, lying close to the BGC, hosts several Au-Cu deposits/prospects in the SGMB viz. Bhukia, Jagpura, Delwara, Dagocha, Ghagri etc. [31]. The Geological Survey of India (GSI) has discovered gold-copper mineralization in the Bhukia area of SGMB in 1993 [49]. The subsequent exploration by the GSI has established 114.78 mt of gold resource with an average grade of 1.95 g/t gold, 0.15% associated copper, 93 g/t nickel and 130 g/t cobalt resource [54]. The interface of the BGC and the Aravalli Supergroup between Delwara and Ghatol in southeastern Rajasthan is mineralized (Cu-Au-iron oxide-graphite), [32]. In SGMB, the deposits/prospects situated in the southern part are more promising gold deposits in Western India [31,32,39,51,55].

The mineralization in this belt is represented by pyrrhotite, chalcopyrite, arsenopyrite, pyrite, loellingite along with magnetite, goethite and native gold. The host rock for auriferous mineralization is carbonate rocks and albitite. The U-Pb zircon ages of albite-rich rock from Bhukia deposit ranges from 1740 to 1820 Ma [56]. Gold-copper mineralization in this belt occurs as disseminations, massive ore, veins, stringers and smears along with shear fractures. The localization of ore is controlled by shears, genetically related to the D_2 phase of deformation. The ore is localized along with hinges of F_2 folds and F_2 axial plane which are parallel to D_2 shear planes. The associated alteration is characterized by pervasive Na-Ca-Mg-Fe-B-Ti alterations [31]. The present work is focused on Jagpura Au-Cu deposit, located in the southern part of the SGMB belongs to the Jagpura Formation of the Debari Group of the Aravalli Supergroup.

3. Deposit Geology

The lithologic units of the Jagpura deposit are classified into two different tectonostratigraphic domains: one is part of the Archean basement known as the Banded Gneissic Complex (BGC) and the other is part of Paleoproterozoic meta-sedimentary units of the Debari Group of the Aravalli Supergroup (Figure 3). The BGC is represented by medium grade staurolite schist, overlain by meta-sedimentary rock sequence comprising of dolomitic marble, amphibole quartzite, quartz-mica schist and albitite of the Jagpura Formation, Debari Group of the Aravalli Supergroup with a tectonic contact.

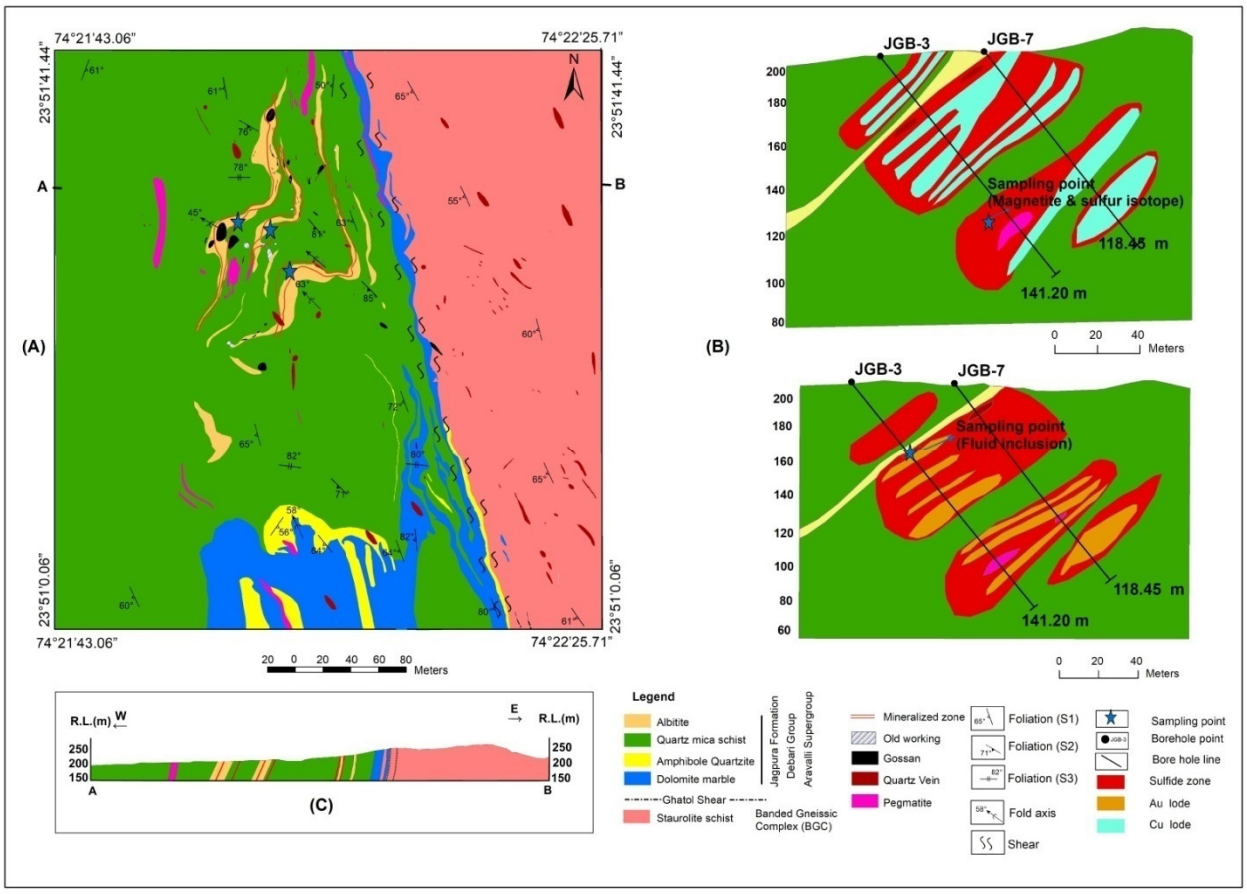

Figure 3. (**A**) Geological map of the Jagpura deposit showing different litho-units and mineralized zones, modified from reference [57], Albitite is from reference [27]; (**B**) longitudinal borehole cross-section showing the position of ore lodes; (**C**) Geological cross-section along line A–B in Figure 3A.

Staurolite schist is asilver-grey to dark grey colored fine to medium grained rock. The contact between staurolite schist and dolomitic marble is sheared, marked by various

kinematic indicators in which sigma structure of quartz porphyroblast indicates a dextral sense of shearing. Dolomitic marble is medium to coarse-grained, fawn colored crystalline rock and exhibits well-developed elephant skin weathering and saccharoidal texture. Amphibole quartzite is exposed in the southern part of the deposit and is brown to pink colored, medium grained, hard and compact rock. It is composed mainly of quartz, actinolite and K-feldspar. Quartz-mica schist is the most dominant lithologic unit in the deposit. It is abuff-grey to greenish-grey colored, fine-grained rock with a silvery sheen at places with more muscovite concentration. The rock shows the development of quartz porphyroblasts, crenulation cleavage, well-developed schistosity marked by a strong preferred orientation of muscovite, chlorite and biotite (Figure 4A). The rock is traversed by foliation parallel magnetite veins and highly ferruginized at places (Figure 4B–D). Albitite is a brown to brick-red colored, fine grained, hard and compact rock (Figure 4E). It occurs as competent bands within quartz-mica schist, contains foliation parallel tourmaline rich bands and ferruginized at places.

Figure 4. Field photograph showing: (**A**) Well-developed foliation in quartz-mica schist; (**B**) Quartz-mica schist is characterized by the presence of foliation parallel magnetite veins; (**C**) Magnetite veins within quartz-mica schist; (**D**) Intense Fe alteration in quartz-mica schist; (**E**) Albitite occurring within quartz-mica schist as competent bands; (**F**) Ferruginized quartz vein within quartz-mica schist; (**G**) Well developed gossan zone within quartz-mica schist; (**H**) Old workings at contact of quartz-mica schist and albitite; (**I**) Malachite staining in wall of old workings; (**J**) Hydrothermal ferruginized breccias within quartz-mica schist indicate brecciation due to hydrothermal activity; (**K**)

Na-B alteration marked by occurrence of albite and tourmaline veins; (**L**) Two generations of quartz veins occurring parallel to S_1 and S_2 foliation, depicting cross cutting relationship with each other.

Intrusive quartz veins are observed in all the lithologic units of the study area. Two generations of quartz veins are observed: the first-generation quartz veins are disposed of parallel to the S_1foliation plane, the second-generation quartz veins are disposed parallel to the S_2 foliation plane and show a cross-cutting relationship with each other (Figure 4L). The second-generation quartz veins are prominent and associated with ore mineralization. The length of these quartz veins varies from 2 cm to 5 m and the width varies from 2 cm to 1 m. The quartz veins are ferruginized at places (Figure 4F). Quartz-mica schist and albitite are also traversed by pegmatite veins. The length of pegmatite veins varies from 5 cm to 4 m and the width varies from 2 to 15 cm. Calcite veins are present in quartz-mica schist, albitite and dolomitic marble lithologic unit and are variable in size ranging from 1 to 20 cm in length and 2 to 10 cm in width. Iron oxides in the deposit are represented by magnetite which occurs ubiquitously within quartz-mica schist and albitite as discontinuous veins parallel to the S_2 foliation plane (Figure 4B,C) and also as disseminations at places. The length of iron oxide veins varies from 15 cm to 2 m and the width varies from 1 to 10 cm.The mineral assemblages in different lithologic units of Jagpura deposit indicate upper greenschist to middle amphibolite facies of metamorphism.

3.1. Structure

The lithologic units of the Jagpura deposit show NNW-SSE to N-S structural trends with moderate (50°) to steep (82°) dip towards WSW and ESE. Three distinct phases of deformation have been identified in the area. F_1 type rootless, isoclinal folds represent D_1 phase deformation. The trends of the first-generation axial traces are NNW-SSE to NW-SE. D_2 phase deformation is marked by symmetrical to asymmetrical, tightly to openly inclined, moderately to steep plunging F_2 folds towards NW. F_2 folds control the outcrop pattern of the area and axial traces strike towards NW-SE. Broad warps with widely spaced fracture cleavage and chevron folds represent the D_3 phase of deformation. The trends of the third-generation axial traces are ENE-WSW to E-W. The third generation of folds is less pervasive and has least affected the outcrop pattern of the area. The contact between basement and cover rock is traversed through a ductile shear zone which is evident from several kinematic indicators along with mylonitic foliation. The sense of shear is dextral. The NNW-SSE trending shear zone is exposed in the eastern side of the study area and is part of the regional Ghatol shear zone. The shear zone is sympathetic to the regional D_2 deformation and shear plane is parallel with S_2 foliation. The ore microscopic studies show that the mineralization is localized along shear plane and fold hinges related to D_2 phase deformation event. In the study area, second-generation quartz veins occurring parallel to S_2 foliation are prominent and associated with mineralization. The fluid inclusion study of mineralized quartz vein suggest that the high saline ore fluids injected during the D_2 phase of deformation is responsible for the transportation of metals in the ore system as metals chloride complex.

3.2. Mineralization

In the Jagpura deposit, surface indications of mineralization are gossan zones, old workings, malachite-azurite stains, hydrothermal alteration, veins and disseminations of iron oxide (magnetite), as well as the presence of visible sulfides (Figure 4G–I). In the study area, 12 old workings are present which are semi-circular in shape and open-pit type. The length of these old workings varies from 08 to10 m and the width varies from 2 to 5 m. Gossan zones are yellow, deep brown to brick-red, massive, hard and compact, and parallel to sub-parallel discontinuous bands. At places, native gold is seen as fine flakes and specks within the gossan zone. Albitite and quartz-mica schist are the host rocks for gold-copper mineralization. Three parallel gold-copper mineralized zones are exposed in the deposit. The cumulative strike length of the mineralized zones is about

1050 m (400 m, 350 m and 300 m), with the width varying from 20 to 30 m.The ore mineral association of the Au-Cu mineralization is native gold, arsenopyrite, loellingite and chalcopyrite with associated pyrrhotite, pyrite and abundant magnetite. Alongside these mineral associations, maldonite (Au_2Bi) and hedleyite (Bi_7Te_3) are also observed as bismuth phases. Apatite, quartz, chlorite, biotite, albite, tourmaline and muscovite are common gangue minerals associated with the Au-Cu ore.

Subsurface mineralization is shallow in nature and all the three mineralized zones have been intersected in drillholes. Four different styles of mineralization are present in drillhole core samples i.e., (1) semi-massive to massive type, (2) vein and fracture fill type, (3) foliation parallel disseminations/smears and (4) patchy and stringer type (Figure 5A–F). The Geological Survey of India (GSI) has augmented a total resource of 6.07 mt gold with an average grade of 1.67 g/t Au and 8.05 mt copper with an average grade of 0.23% Cu [34,58]. Gold-copper mineralized zones occur along the hinges of F_2 fold and F_2 axial planes parallel to the D_2 shear planes. The mineralization is also observed in epigenetic quartz and pegmatite veins (Figure 5G,H).

3.3. Alteration Pattern

Hydrothermal alteration in the Jagpura deposit is represented by pervasive Na-B alteration besides chloritization, sericitization, silicification, ferruginization and hydrothermal iron oxide breccias present close to the gold-copper mineralized zones. In the Jagpura deposit,hydrothermal alteration is dominated by Na-B metasomatism (Figure 4K), marked by the ubiquitous presence of albite and tourmaline in all the lithologic units of the Jagpura Formation [34,35]. In the study area, B metasomatism postdates Na metasomatism. Within quartz-mica schist, Na metasomatism was so intense that it has formed albitite rock. Silicification is present along the S_1 and S_2 foliation. However, quartz veins occurring parallel to the S_2 foliation are dominant and close to the ore zones. Chloritization (of biotite and amphibole) near sulfide mineralization is mainly associated with the shear zone Calcic alteration is marked by the presence of calcite veins besides tremolite, actinolite (calcic amphibole) and oligoclase, andesine mineral assemblages. A lesser degree of K-alteration is also observed along the shear planes marked by biotite enrichment and albite replacement by K-feldspar. Alteration of feldspar to sericite is noted throughout the host rocks Intense ferruginization (magnetite, goethite) is present in the quartz-mica schist, albitite and in quartz veins. Hydrothermal iron oxide breccia occurs in patches within the host rock. It is composed of rounded to angular clasts made up of polycrystalline quartz set in a ferruginized matrix (Figures 4J). The occurrence of albite, tourmaline, magnetite, chlorite, actinolite, tremolite, calcite and sphene represents Na-B-Fe-Mg-Ca-K alteration within the host rock proximal to Au-Cu ore zones.

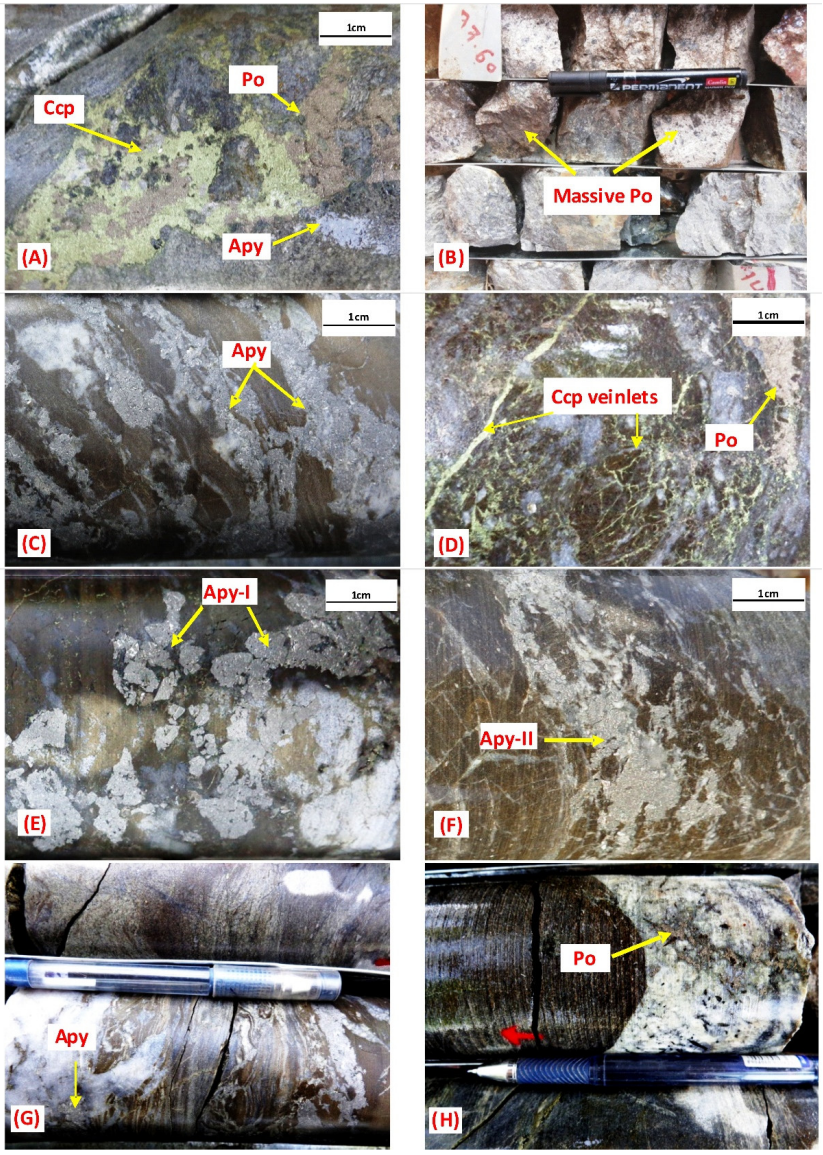

Figure 5. Photograph of drill core showing nature of sulfide mineralization in the Jagpura deposit. (**A**) Association of pyrrhotite, chalcopyrite and arsenopyrite in borehole core; (**B**) Massive to semi massive type pyrrhotite mineralization; (**C**) Foliation parallel semi massive arsenopyrite; (**D**) Vein and fracture filled chalcopyrite, pyrrhotite and arsenopyrite; (**E**) Euhedral coarse grained arsenopyrite specks of first generation; (**F**) Fine grained massive arsenopyrite of second generation; (**G**) Second generation arsenopyrite in quartz vein; (**H**) Stringers of pyrrhotite and disseminations of arsenopyrite in pegmatite vein. (Apy = arsenopyrite, Po = pyrrhotite, Ccp = chalcopyrite).

4. Materials and Methods

4.1. Sampling

For petrography, mineral chemistry, fluid inclusion, and sulfur isotope study, samples were collected from the Jagpura deposit of the SGMB. Both surface and drill core samples of host rocks and ore zones were collected for analysis (Figure 3). Samples from all stages of ore formation, representing different ore and gangue mineral assemblages, were collected. These samples were used for petrographic study and representative samples were used for electron probe micro analyzer (EPMA). Auriferous quartz vein (n = 10) occurring parallel to S_2 foliation was sampled for fluid inclusion study. A pure fraction of sulfides viz. pyrite, arsenopyrite, pyrrhotite and chalcopyrite were collected from the different ore zones for sulfur isotope analysis.

4.2. Petrography and EPMA

Thin polished and polished sections of host rocks (n = 25) were studied for ore mineralogical and petrological studies using Leica DMRX advanced polarizing petrological microscope at the Regional Petrology Laboratory, the Geological Survey of India, Jaipur, India. Representative sections (n = 10) were studied to determine the mineral chemistry and to understand the nature of the gold and sulfide mineral phases using Electron Probe Micro Analyzer (EPMA), CAMECA SX-100 with five wave dispersive spectrometers (WDS) at National Centre of Excellence in Geoscience Research (NCEGR), GSI, Faridabad, India. The polished thin sections were examined using an optical microscope to characterize the mineralogical and textural relationship of the ore and associated gangue minerals. EPMA analysis was carried out using the operating column conditions of 20 kv accelerating voltage and a probe current of 15nA. Analyses were carried out using a beam diameter of 1 μm. Peak and background counting times for major elements were 20 s and 10 s, respectively, whereas those for trace elements were 40 s and 20 s, respectively. Natural standards were run before and after analysis to determine the analytical error. Two sections were studied to determine the mineral chemistry of magnetite using Electron Probe Micro Analyzer (EPMA), CAMECA SX-5 at Central Research Facilities in Indian Institute of Technology (Indian School of Mines), Dhanbad, India. The analyses were carried out for Si, Ti, Al, Fe, Mn, Mg, Ca, Na, K, Ni, Co, V and Cr using the operating column conditions 15 kv accelerating voltage, probe current of 12 nA and beam diameter of 1 μm. Standards were run before and after analysis to determine the analytical error. The standards used for calibration of the instrument are as follows: spinel for Mg and Al, ilmenite for Ti, vanadium metal for V, chromite for Cr and Fe, and manganese oxide for Mn. Vanadium concentrations were corrected for the overlap between Ti K_β and V $K\alpha$ peaks by analyzing V-free and Ti bearing standards of rutile and metallic Ti. Matrix correction was carried outusing the ZAF correction. The analytical inaccuracies and uncertainties of the analysis are negligible and as follows: <0.1% for Cr; <1% for Al, Si, K, Ca, Fe, Mg, Ti, Co, V; <2% for Mn and Na.

4.3. Fluid Inclusion Micro Thermometry

At the Fluid Inclusion Lab of NCEGR, GSI, Bengaluru, India, the fluid inclusions were observed under a microscope at high magnification and the temperatures of thermally induced phase transitions in fluid inclusions were evaluated using a calibrated LINKAM THMSG 600 heating/freezing stage. The heating and freezing stage is equipped with an Olympus BX-50 transmitted light microscope, an LNP-95-LTS liquid nitrogen chilling unit, and a digital video capturing system for temperature monitoring. LINKSYS is the program used to study fluid inclusions. The system was calibrated, and the reproducibility of measurements at room temperature was tested using natural fluid inclusion standards from quartz crystals tested in other established laboratories, as well as LINKAM's standard CO_2 standards, with reproducibility achieved within the standard accepted error limits. The apparatus operates at temperatures ranging from 196 to 600 °C.

4.4. Sulfur Isotopic Composition

A total of 31 sulfide samples were selected for conducting the sulfur isotope studies and the respective data were generated from the Isotope Ratio Mass Spectrometry (IRMS) laboratory, NCEGR, GSI, Bengaluru, India. Sulfide grains were separated by hand from gangue minerals under a stereomicroscope and then powdered avoiding any contamination. Using the ANCA GSL (Automated Nitrogen and Carbon Analyzer for Gas Solids and Liquid) peripheral system; the separated powdered samples were analyzed for sulfur isotopes in continuous flow mode using an Isotope Ratio Mass Spectrometer (Make: SerCon, Model: Geo 2020). Around 3550 mg powder of each sulfide mineral was manually packed into tin capsules and placed into the auto-sampler unit above the ANCA, with the positions noted. Each tin capsule was put one by one into a furnace at 1050 °C with an

additional oxygen pulse during the analysis. In the presence of oxygen, the tin ignites and burns exothermally, raising the temperature to around 1800 °C and oxidizing the sample. Water is removed using a Nafion dryer and anhydrous magnesium perchlorate trap. Helium is the carrier gas used (99.99%). The gas stream is routed through a gas chromatograph, where sulfur is separated and injected into a mass spectrometer for isotope analysis of sulfur. Each sample's total analysis time is 9 m 10 s. Analytical techniques and fractionation mechanism was followed in accordance with [59,60]. Each sample was analyzed three times in a batch, along with international reference (NBS) and internal laboratory standards. All sulfur-bearing samples are measured using the VCDT scale [61].

4.5. Geochemical Analysis

For geochemical analysis, drill core samples (n = 10) were collected from mineralized zone. The samples were crushed to -100 mesh size, sieved, coned and quartered, for major, trace, base metal and REE analysis. The geochemical analysis was carried out at NABL accredited (ISO/IEC17025:2005) chemical laboratory of Geological Survey of India, Western Region, Jaipur.The trace elements including REE were analyzed using Varian 820 Inductively Coupled Plasma Mass Spectrometry (ICP-MS instrument, following the closed digestion sample preparation technique). Standard reference materials (SRMs) were employed to estimate accuracy and precision of the instrument. Gold was analyzed using fire assay technique with ICPMS/GTAAS instrument. The base metal (Cu, Ni, Co, Pb, Zn) was analyzed using Flame Atomic Absorption Spectrophotometer (FAAS, Agilent Duo 280 AAS) instrument. The samples were pulverized to −200 mesh size using vibratory cup mill and taken in tightly packed zip plastic bag. For digestion, 0.2 g of the sample was weighed in a test tube and 5 mls of HNO3: HCl mixture in 1:2 ratios were added to it. The solution was heated over hotplate for 4 h and then made up with Type-I water and allowed to settle. The final solution was used for the determination of Cu, Ni, Co, Pb, Zn.

5. Results

5.1. Petrography and EPMA Study

5.1.1. Petrography of Host Rocks

Detailed petrographic studies of gangue and ore minerals of the host rocks were carried out to understand the relationship between gangue and ore minerals, nature of gold mineralization, microstructures, mineral paragenesis and hydrothermal alteration pattern. Quartz-mica schist is composed of muscovite, chlorite, sericite and quartz with an accessory amount of apatite, feldspar, tourmaline, biotite, ilmenite, rutile, hornblende, orthoclase and sphene (Figure 6A–F). A few sections also observe the alteration of biotite and amphibole to chlorite. The rock shows well-developed schistosity, marked by the parallel alignment of chlorite, muscovite, and sericite. S-C fabric, mica fish and pressure shadow are also observed within the rock. Orientation of mica fish and S-C fabric shows a dextral sense of shearing (Figure 6J) and alteration of feldspar to sericite. (Figure 6K). The rock shows well-developed crenulation cleavage and microfolds associated with the second phase of deformation. In chlorite, Fe/Fe+Mg ratio varies from 0.42 to 0.61 and Mg/Fe + Mg ratio ranges from 0.39 to 0.58. Most chlorites are ripidolite with few pynochlorite and diabantite (Figure 8E). Feldspar is mostly albite ($Ab_{98.6\text{-}91}An_{8.2\text{-}0.4}Or_{3\text{-}0.1}$) to oligoclase [($Ab_{84.8\text{-}70.9}An_{27.1\text{-}14.6}Or_{2\text{-}0.3}$), (Figure 8F) and tourmaline is dravite variety.

Albitite comprises albite ($Ab_{98.7\text{-}90.8}An_{9.1\text{-}0.7}$) and tourmaline as major minerals (Figure 6D) along with apatite, biotite, muscovite, actinolite, quartz, orthoclase, rutile and ilmenite as accessory minerals. Albite occurs as subhedral, polygonal grains and generally untwined in nature. In some sections, albite constitutes up to 90% volume of the rock. Tourmaline occurs as euhedral to subhedral grains and shows strong pleochroism in brown shades. The concentration of tourmaline ranges from 5 to 50% volume of the rocks. A higher concentration of tourmaline is observed in the mineralized zones. Albite and

tourmaline grains in albitite are elongated and aligned, parallel to the shear foliation close to the shear zone (Figure 6G,H).

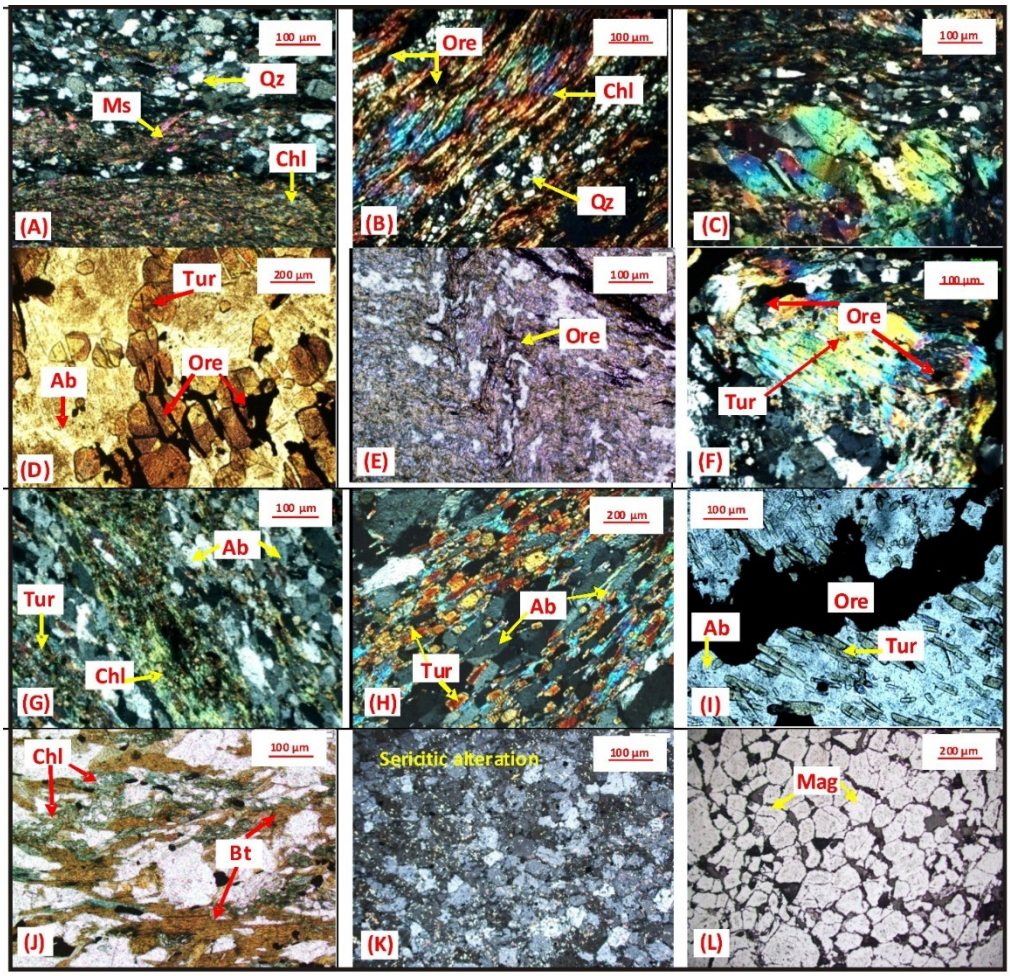

Figure 6. Photomicrograph showing mineral assemblages related to alteration zones, D_2 deformation and shear system. (**A**) Quartz-mica schist is mainly consists of muscovite, chlorite and quartz; (**B**) Alternate bandings of quartz and chlorite rich layers within quartz-mica schist; (**C**) Mica fish structure within quartz-mica schist indicating dextral nature of the shear zone; (**D**) Gold-sulfide mineralization is associated with extensive hydrothermal alterations viz. albitization and tourmalinization, also to note that mineralization is occurring parallel to the fractures of tourmaline grains; (**E**,**F**) F_2 fold in quartz-mica schist with disposition of opaque minerals at the hinge; (**G**,**H**) Elongated albite and tourmaline grains in albitite close to shear zone; (**I**) Sulfide vein cross cutting the foliation of albite-tourmaline grains in albitite; (**J**) Alteration of biotite to chlorite in proximity to sulfide disseminations; (**K**) Sericitic alteration in albitite (PPL); (**L**) Angular grains of magnetite within iron oxide breccia. (Mag = magnetite, Ms = muscovite, Qz = quartz, Chl = chlorite, Ab = albite, Tur = tourmaline, PPL = plane polarized light).

5.1.2. Ore Petrography and Ore Chemistry

The sulfide mineral assemblages of the Jagpura deposit are represented by pyrrhotite, chalcopyrite, arsenopyrite, loellingite and pyrite in the order of abundance (Figure 7A–O). Moreover, native gold, maldonite (Au_2Bi) and hedleyite (Bi_7Te_3) are present as gold and bismuth ore, respectively (Figure 8D). The sulfide minerals occur as semi-massive to massive type, vein and fracture fill type, foliation parallel type, patchy and stringers type. Magnetite is the dominant oxide phase and is closely associated with gold-sulfide mineralization (Figure 7G,J,M); it is euhedral to subhedral in shape and occurs as disseminations and veins (Figures 7E,I,M and 8A,B). Apatite is euhedral, hexagonal in shape and occurs as disseminations parallel to the foliation plane of host rocks (Figure 7L). Apatite

is associated with magnetite and chalcopyrite at many places (Figures 7L and 8C). The ore minerals indicate replacement, remobilization and deformational textures. Major sulfide phases show replacement textures. Two types of arsenopyrite are observed in the ore zones: one is coarse grained, granular and intensely fractured with cataclastic texture (Figure 7A) and the other is idiomorphic, euhedral, rhombic in shape, fine to medium grained without deformation texture (Figure 7B). The healing of fractures within the arsenopyrite by chalcopyrite shows that the former is replaced by the later (Figure 7C). The convexity of chalcopyrite grain boundary within pyrrhotite shows that pyrrhotite has formed earlier (Figure 7D). Occurrence of sulfides along weak planes viz. fractures, veins and shear planes (Figure 7H,K) and the hinge of F_2 folds represents ore remobilization (Figures 6E,F and 7F). In mineralized zones, sulfide veins cross-cutting the albite-tourmaline grains (Figure 6I), deformed albite twin lamellae and cataclastic fragments of sulfide minerals indicate ore deformational textures (Figure 7K). Sulfide minerals such as pyrite and arsenopyrite are associated with gold [62]. Arsenopyrite has a higher gold content than pyrite, and the gold content of arsenian pyrites increases with arsenic content [63].

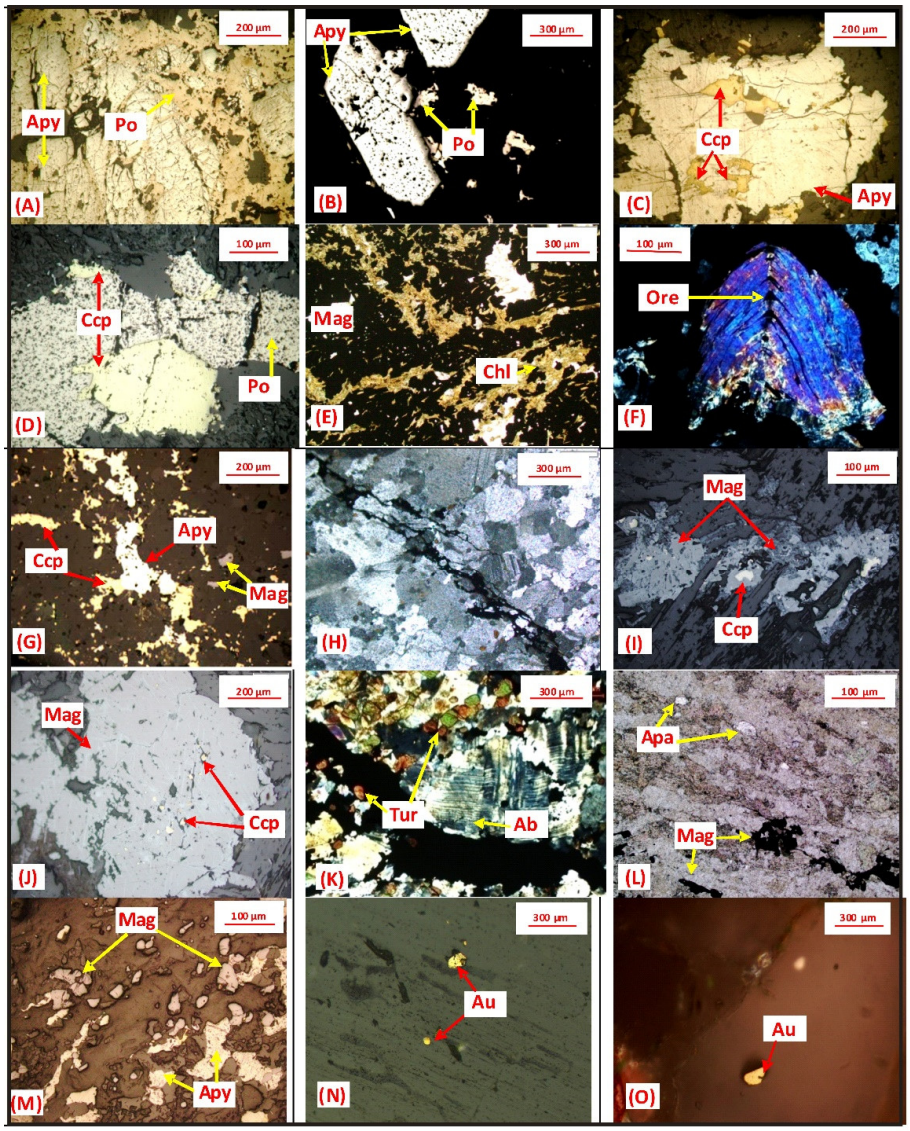

Figure 7. Photomicrograph showing various generations of mineral assemblages such as magnetite-apatite-sulfides-gold and their linkages to the shear zone characteristics and deformation patterns. (**A**) Catascatically deformed arsenopyrite of the first generation, where fractures are healed by pyrrhotite; (**B**) Undeformed isomorphic, euhedral, rhombic shaped second generation arsenopyrite; (**C**) Fractures of arsenopyrite are healed by later formed chalcopyrite; (**D**) Convexity of chalcopyrite

grain in pyrrhotite indicate that pyrrhotite has formed earlier; (**E**) Occurrence of abundant subhedral magnetite grains within quartz-mica schist; (**F**) Saddle reef structure having sulfide mineralization at the hinge of microfold indicating ore remobilization; (**G**) Disseminations of arsenopyrite, pyrrhotite, chalcopyrite and magnetite of early stage mineralization; (**H**) Nature of mineralized shear system showing shear planes cross cutting the albite grains; (**I**) Magnetite vein of second stage mineralization, occurring parallel to shear fracture; (**J**) Coarse grained magnetite with associated chalcopyrite; (**K**) Deformed albite twin lamellae in albitite close to mineralized vein; (**L**) Occurrence of subhedral apatite grains associated with magnetite in quartz-mica schist; (**M**) Disseminated magnetite and arsenopyrite of early stage mineralization; (**N**) Native gold grains in quartz-mica schist; (**O**) Skeletal gold speck in second generation quartz vein intrusive within quartz-mica schist. (Apa = apatite, Mag = magnetite, Apy = arsenopyrite, Po = pyrrhotite, Ccp = chalcopyrite, Au = gold, Tur = tourmaline, Ab = albite, Chl = chlorite).

Ore petrography revealed that gold is mainly present within the arsenopyrite and loellingite. Within the arsenopyrite, gold occurs in association with loellingite, maldonite and hedleyite. Gold occurs as specks, fine flakes and films varying in size from a fraction of a micron to 40 microns (Figure 7N). Gold also occurs along the fractures within the arsenopyrite and loellingite. Epigenetic quartz vein within the host rocks also contains native gold (Figure 7O). Arsenopyrite and loellingite are intimately associated and form the main gold bearing minerals in the study area. EPMA analysis of native gold indicates that Au concentration ranges from 89.25 to 94.72 wt% and it contains silver as a minor impurity (6.15 to 8.46 wt%). Gold fineness ranges from 914–937‰, with average value of 927‰ (n = 6).

EPMA analysis of the sulfides also indicates the presence of invisible gold. Gold content ranges from 0.02 to 2.58 wt% in arsenopyrite, 0.02 to 0.20 wt% in chalcopyrite, 0.08 to 0.11wt% in pyrrhotite and up to 0.17 wt% in loellingite. The EPMA study reveals that loellingite and arsenopyrite occur as coexisting phase within the ore zones. However, loellingite is the preferred residence for gold mineralization compared to arsenopyrite (Figure 8D). Arsenic content is higher in loellingite (72.20 to 72.36 wt%) than arsenopyrite (47.07 to 51.05 wt%). Loellingite and arsenopyrite are also rich in nickel and cobalt wherein, loellingite shows higher values compared to arsenopyrite [Table 1]. The nickel and cobalt values in loellingite range from 2.10 to 2.45 wt% and 1.08 to 1.44 wt%, respectively. The nickel and cobalt values in arsenopyrite are 0.39 to 2.22 wt% and 0.18 to 0.40 wt%, respectively.

Table 1. EPMA data of Au, Au-Te, Au-Bi and sulfide phases (in Wt%) from the Jagpura gold-copper deposit, western India.

Lithology: Albitite, Sample No. JGB-10													
Mineral Name	**Gold (Au)**			**Arsenopyrite (FeAsS)**			**Pyrrhotite (FeS)**			**Chalcopyrite ($CuFeS_2$)**			
EPMA Analysis No.	1/1	1/2	1/3	1/4	1/5	1/6	1/7	1/8	1/9	1/10	1/11	1/12	1/13
S	0.09	0.02	0.02	17.74	17.70	17.33	38.27	39.04	39.17	34.14	34.18	34.03	33.88
Fe	0.68	0.12	0.12	31.10	31.60	34.68	59.85	58.75	59.22	30.08	29.35	30.02	29.92
Co	bdl	bdl	0.02	2.22	0.88	0.39	0.01	0.03	bdl	bdl	0.01	bdl	0.03
Ni	0.10	bdl	bdl	0.40	0.29	bdl	0.07	0.04	bdl	bdl	0.03	bdl	bdl
Cu	0.08	0.02	0.01	bdl	0.02	0.03	0.01	0.01	0.01	32.66	33.79	32.6	33.02
Zn	bdl	0.10	0.02	bdl	bdl	bdl	bdl	bdl	bdl	bdl	0.02	0.05	0.02
As	0.25	0.08	0.01	48.10	49.14	47.07	bdl	0.02	bdl	bdl	0.04	bdl	bdl
Mo	bdl	bdl	bdl	bdl	0.24	0.22	0.51	0.56	0.49	0.46	0.50	0.43	0.58
Ag	7.20	6.15	6.58	0.03	bdl	0.04	bdl	bdl	0.02	0.08	bdl	bdl	bdl
Cd	0.14	0.02	0.08	bdl	0.01	bdl	bdl	0.02	bdl	bdl	0.06	bdl	bdl

Te	bdl	bdl	bdl	bdl	bdl	bdl	bdl	0.02	bdl	2.44	bdl	2.42	2.19
Au	89.95	92.12	92.21	0.13	0.06	0.07	0.11	0.08	0.10	0.10	0.20	0.06	0.02
Pb	bdl	bdl	bdl	0.15	bdl	0.13	bdl	bdl	bdl	bdl	0.13	bdl	bdl
Bi	bdl	bdl	bdl	0.10	bdl	bdl	bdl	bdl	bdl	bdl	bdl	bdl	bdl
Total	98.49	98.63	99.07	99.97	99.94	99.96	98.83	98.57	99.01	99.96	98.31	99.61	99.66
Lithology: Quartz-mica schist, Sample No. JGB-7													
Mineral Name	**Gold (Au)**			**Loellingite ($FeAs_2$)**			**Maldonite (Au_2Bi)**		**Hedleyite (Bi_7Te_3)**		**Arsenopyrite (FeAsS)**		
EPMA Analysis No.	1/1	1/2	1/3	1/4	1/5	1/6	1/7	1/8	1/9	1/10	1/11	1/12	
S	0.05	0.07	0.01	1.29	1.17	1.30	0.07	bdl	0.04	0.02	16.65	18.25	
Fe	0.22	0.72	0.21	24.71	24.06	24.38	1.52	0.32	0.32	0.30	31.03	32.13	
Co	bdl	bdl	bdl	1.08	1.44	1.41	0.06	0.04	0.07	0.09	0.69	0.67	
Ni	0.01	0.11	0.05	2.45	2.50	2.10	0.11	0.06	0.14	0.15	0.29	0.18	
Cu	0.03	0.07	0.04	bdl	bdl	bdl	bdl	bdl	bdl	bdl	bdl	bdl	
Zn	bdl	bdl	bdl	bdl	bdl	bdl	bdl	bdl	bdl	bdl	bdl	0.02	
As	0.08	0.21	0.03	70.36	70.20	70.34	0.32	0.22	0.49	0.42	47.55	48.32	
Mo	bdl	bdl	bdl	0.02	bdl	0.04	bdl	bdl	bdl	bdl	0.19	0.28	
Ag	8.46	7.60	7.12	bdl	0.08	bdl	0.12	0.09	bdl	bdl	0.02	bdl	
Cd	0.03	0.12	bdl	bdl	bdl	bdl	0.19	0.12	bdl	bdl	bdl	0.07	
Te	bdl	bdl	bdl	bdl	bdl	bdl	bdl	bdl	20.39	21.30	0.05	bdl	
Au	89.93	89.25	91.12	bdl	bdl	0.17	64.71	66.47	bdl	bdl	2.58	0.02	
Pb	bdl	bdl	bdl	bdl	bdl	0.11	bdl	bdl	0.10	0.08	bdl	bdl	
Bi	bdl	bdl	bdl	bdl	bdl	bdl	32.68	31.52	78.11	77.18	0.80	bdl	
Total	98.81	98.15	98.58	99.91	99.45	99.85	99.78	98.84	99.66	99.54	99.85	99.94	
Lithology: Quartz-mica schist, Sample No. JGB-8													
Mineral Name	**Pyrite (FeS_2)**												
EPMA Analysis No.	1/1	1/2	1/3	1/4	1/5	1/6	1/7	1/8	1/9	1/10	1/11		
S	53.00	53.25	53.11	53.25	52.49	53.15	52.86	53.13	53.00	53.11	53.25		
Fe	45.88	45.62	46.25	45.62	46.33	46.36	45.80	46.34	45.88	45.25	45.62		
Co	0.06	0.15	0.10	0.15	0.04	0.03	0.19	0.07	0.06	0.10	0.15		
Ni	0.03	0.06	0.04	0.06	0.03	0.02	0.10	0.06	0.03	0.03	0.06		
Cu	bdl	bdl	0.02	bdl	bdl	0.02	0.02	0.01	bdl	0.02	bdl		
Zn	bdl	0.04	bdl	0.04	0.03	bdl	bdl	bdl	bdl	bdl	0.04		
As	bdl	0.01	bdl	0.01	bdl	0.01	0.01	0.02	bdl	bdl	0.01		
Ag	0.01	0.02	0.04	0.02	bdl	0.04	bdl	0.03	0.01	0.04	0.02		
Total	98.99	99.17	99.53	99.16	99.11	99.82	98.99	99.96	99.33	99.13	99.61		
Co/Ni	1.96	2.54	2.40	2.54	1.17	1.76	1.89	1.17	1.96	3.20	2.54		
S/Fe	1.16	1.17	1.15	1.17	1.13	1.15	1.15	1.15	1.16	1.17	1.17		
Fe/(S+As)	0.87	0.86	0.87	0.86	0.88	0.87	0.87	0.87	0.87	0.85	0.86		
bdl = below detection limit													

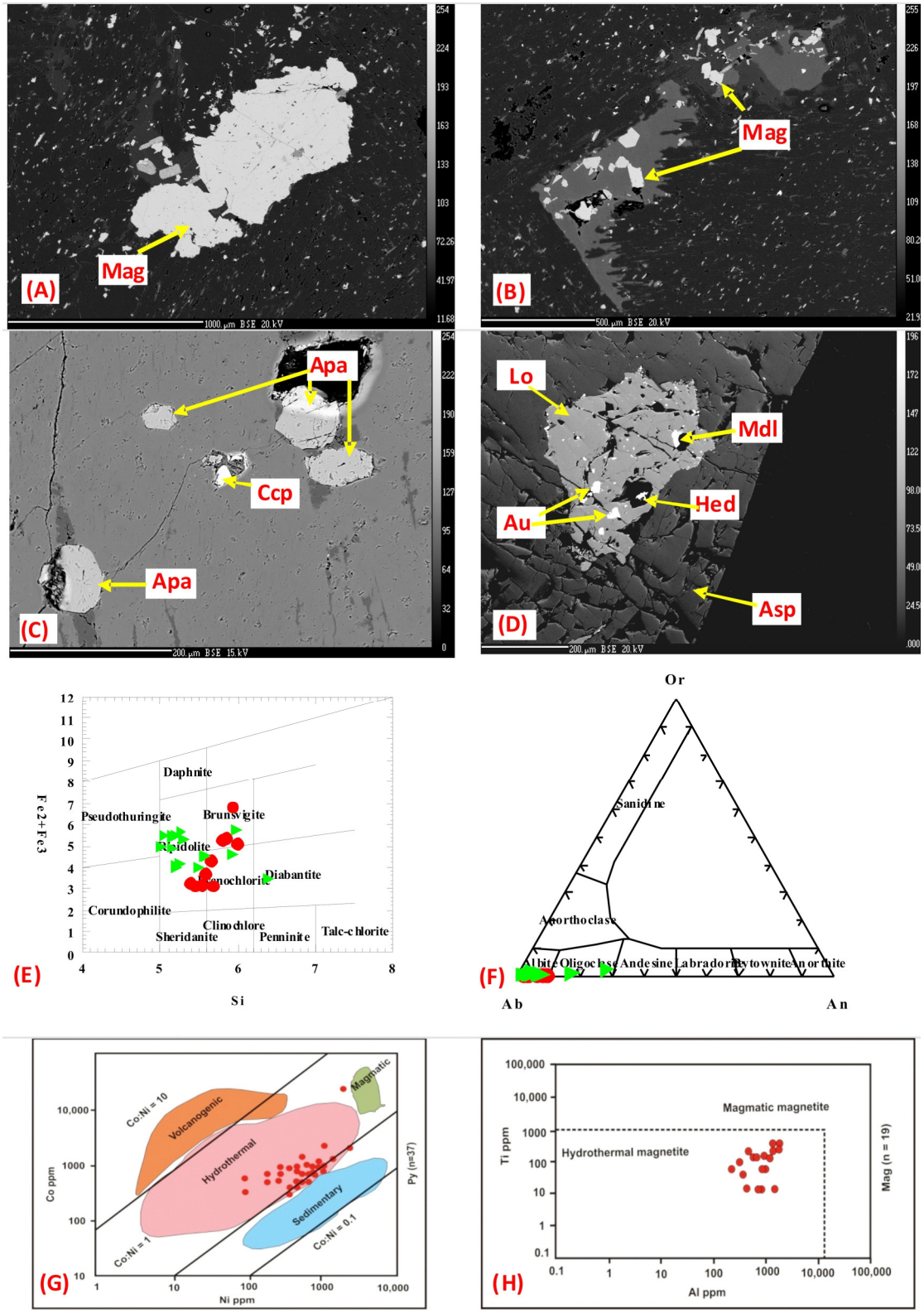

Figure8. BSE images of magnetite-apatite-gold-sulfide mineral assemblages along with plots suggesting hydrothermal nature of pyrite and magnetite in the study area. (**A**) Magnetite megacryst in quartz-mica schist; (**B**) Disseminated magnetite within quartz mica-schist; (**C**) Subrounded to rounded apatite grains associated with chalcopyrite; (**D**) Association of gold, loellingite, arsenopyrite, maldonite and hedleyite; (**E**) Mineral composition classification diagram of chlorite, (Red = albitite, green = quartz-mica schist); (**F**) Or-Ab-An classification diagram of feldspar. (Red = albitite, green = quartz-mica schist); (**G**) Co vs. Ni plot of pyrite show hydrothermal signature, fields for pyrite composition from references [64]; (**H**) Ti vs. Al covariation plots of magnetite indicates

magnetite is hydrothermal in nature, fields from reference [65]. (Apa = apatite, Mag = magnetite, Ccp = chalcopyrite, Au = gold, Mdl = maldonite, Lo = loellingite, Hed = hedleyite).

The EPMA study of magnetite from the study area reveals that the concentrations of TiO_2 ranges from(0.01 to 0.11 wt%), Al_2O_3 (0.06 to 0.28 wt%), MnO (up to 0.01 wt%), FeO (83.39 to 89.02 wt%), MgO (0.01 to 0.08 wt%), V_2O_3 (0.03 to 0.26 wt%), Cr_2O_3 (0.01 to 0.09 wt%), NiO (0.04 to 0.31 wt%), CoO (0.02 to 0.05 wt%) and CaO (0.01 to 0.08 wt%) [Table 2]. Magnetite shows low concentrations of TiO_2 (0.01 to 0.11 wt%) and Al_2O_3 (0.06 to 0.28 wt%). The Co/Ni ratio of magnetite is <1 (0.04 to 0.67) and Ni/Cr ratio is ≥1 (1 to 4). Co/Ni ratio of pyrite from the study area is >1 (1 to 2.54, n = 22). The EPMA analysis of apatite reveals that apatite is of fluorapatite variety with F content >1 wt% and >1F/Cl ratio [Table 3]. Apatite has a higher concentration of F (4.23 to 5.97 wt%, n = 10) and a lower concentration of Cl (0.08 to 0.73 wt%), FeO (0.01 to 0.28 wt%), and MnO (0.01 to 0.07 wt%).

Table 2. EPMA data of magnetite from the Jagpura gold-copper deposit, western India.

Lithology: Quartz-mica Schist, Sample No. JGB-8										
Mineral Name	**Magnetite**									
EPMA Analysis No.	1/1	1/2	1/3	1/4	1/5	1/6	1/7	1/8	1/9	1/10
Wt%										
SiO_2	0.02	0.17	0.06	0.10	0.02	bdl	0.05	0.04	0.10	0.06
TiO_2	0.05	0.01	0.05	0.07	0.01	0.10	0.05	0.09	0.01	0.05
Al_2O_3	0.12	0.14	0.13	0.11	0.10	0.28	0.15	0.27	0.26	0.21
Cr_2O_3	0.05	0.06	0.04	0.05	0.07	0.06	0.07	0.04	0.05	0.03
V_2O_3	0.20	0.17	0.18	0.07	0.17	0.15	0.08	0.15	0.19	0.17
FeO	89.02	87.69	88.49	87.88	87.82	83.39	83.82	88.57	86.63	88.98
MnO	bdl	0.06	bdl	0.06	bdl	0.01	0.03	bdl	bdl	bdl
MgO	0.05	0.08	bdl	bdl	0.03	bdl	0.01	bdl	bdl	bdl
CaO	bdl	0.03	bdl	bdl	bdl	0.01	0.02	bdl	0.02	bdl
Na_2O	0.02	0.01	0.05	0.03	bdl	0.08	0.01	0.01	0.01	0.05
K_2O	0.04	0.03	bdl	bdl	bdl	0.02	bdl	0.01	0.02	bdl
NiO	0.05	0.05	0.05	0.06	0.07	0.05	0.06	0.07	0.05	0.05
CoO	0.02	0.03	0.02	0.03	0.04	0.02	0.03	0.04	0.02	0.02
Total	89.64	88.53	89.07	88.46	88.33	84.17	84.38	89.29	87.36	89.62
apfu Number of ions on the basis of 4 (O)										
Si	0.01	0.08	0.03	0.05	0.01	bdl	0.02	0.02	0.05	0.03
Ti	0.03	0.01	0.03	0.04	0.01	0.06	0.03	0.05	0.01	0.03
Al	0.06	0.07	0.07	0.06	0.05	0.15	0.08	0.14	0.14	0.11
Cr	0.03	0.04	0.03	0.03	0.05	0.04	0.05	0.03	0.03	0.02
V	0.11	0.10	0.10	0.04	0.10	0.08	0.04	0.08	0.11	0.10
Fe	69.20	68.16	68.78	68.31	68.26	64.82	65.15	68.85	67.34	69.17
Mn	bdl	0.05	bdl	0.05	bdl	0.01	0.02	bdl	bdl	bdl
Mg	0.03	0.05	bdl	bdl	0.02	bdl	0.01	bdl	bdl	bdl
Ca	bdl	0.02	bdl	bdl	bdl	0.01	0.01	bdl	0.01	bdl
Na	0.01	0.01	0.04	0.02	bdl	0.06	0.01	0.01	0.01	0.04
K	0.03	0.02	bdl	bdl	bdl	0.02	bdl	0.01	0.02	bdl
Ni	0.04	0.04	0.04	0.05	0.06	0.04	0.05	0.06	0.04	0.04
Co	0.01	0.02	0.01	0.02	0.03	0.01	0.02	0.03	0.01	0.01
Co/Ni	0.25	0.50	0.25	0.40	0.50	0.25	0.40	0.50	0.25	0.25

Ni/Cr	1.18	1.00	1.48	1.67	1.20	1.00	1.06	2.00	1.18	1.95
Lithology: Albitite No. JGB-10										
Mineral name	**Magnetite**									
EPMA Analysis No.	1/1	1/2	1/3	1/4	1/5	1/6	1/7	1/8	1/9	
Wt%										
SiO_2	0.10	0.10	0.02	0.04	0.01	0.03	0.03	0.09	0.03	
SiO_2	0.10	0.10	0.02	0.04	0.01	0.03	0.03	0.09	0.03	
TiO_2	0.03	0.03	0.06	0.04	0.11	0.02	0.03	0.07	0.01	
Al_2O_3	0.17	0.19	0.19	0.08	0.25	0.09	0.06	0.25	0.17	
Cr_2O_3	0.04	0.08	0.07	0.01	0.06	0.09	0.04	0.09	0.09	
V_2O_3	0.15	0.12	0.26	0.20	0.13	0.13	0.16	0.03	0.08	
FeO	86.27	88.91	85.43	88.23	87.69	87.28	88.19	84.06	88.37	
MnO	bdl	bdl	bdl	bdl	0.10	0.06	0.03	bdl	0.09	
MgO	0.04	bdl	0.01	bdl	bdl	bdl	bdl	0.01	bdl	
CaO	0.04	bdl	0.04	bdl	bdl	0.01	bdl	0.05	bdl	
Na_2O	bdl	0.08	0.03	0.03	0.02	bdl	0.01	0.02	0.01	
K_2O	bdl	bdl	0.02	bdl	bdl	0.01	0.03	bdl	0.01	
NiO	0.04	0.07	0.09	0.05	0.09	0.09	0.04	0.31	0.14	
CoO	0.02	0.05	0.02	0.03	0.05	0.04	0.02	0.02	0.04	
Total	86.90	89.63	86.24	88.71	88.51	87.85	88.64	85.00	89.04	
apfu Number of ions on the basis of 4 (O)										
Si	0.05	0.05	0.01	0.02	bdl	0.01	0.01	0.04	0.01	
Ti	0.02	0.02	0.04	0.02	0.07	0.01	0.02	0.04	0.01	
Al	0.09	0.10	0.10	0.04	0.13	0.05	0.03	0.13	0.09	
Cr	0.02	0.05	0.05	0.01	0.04	0.06	0.02	0.06	0.06	
V	0.08	0.07	0.15	0.11	0.07	0.07	0.09	0.02	0.04	
Fe	67.06	69.11	66.41	68.58	68.16	67.84	68.55	65.34	68.69	
Mn	bdl	bdl	bdl	bdl	0.08	0.05	0.02	bdl	0.07	
Mg	0.02	bdl	0.01	bdl	bdl	bdl	bdl	0.01	bdl	
Ca	0.03	bdl	0.03	bdl	bdl	0.01	bdl	0.04	bdl	
Na	bdl	0.06	0.02	0.02	0.01	bdl	0.01	0.01	0.01	
K	bdl	bdl	0.02	bdl	bdl	0.01	0.02	bdl	0.01	
Ni	0.03	0.06	0.07	0.04	0.07	0.07	0.03	0.24	0.11	
Co	0.01	0.04	0.01	0.02	0.04	0.03	0.01	0.01	0.03	
Co/Ni	0.33	0.67	0.14	0.50	0.57	0.43	0.33	0.04	0.27	
Ni/Cr	1.50	1.20	1.40	4.00	1.75	1.17	1.50	4.00	1.83	

Table 3. EPMA data of apatite (in Wt%) from the Jagpura gold-copper deposit, western India. Lithology: Quartz-mica schist, Sample No. JGB-11.

Mineral Name	**Apatite**						
EPMA Analysis No.	1/1	1/2	1/3	1/4	1/5	1/6	1/7
SiO_2	0.04	0.21	0.04	0.06	0.53	0.04	0.23
TiO_2	bdl	bdl	0.07	bdl	bdl	0.19	bdl
Al_2O_3	bdl	0.02	bdl	0.01	0.07	0.01	0.03
Cr_2O_3	bdl	0.12	0.03	bdl	bdl	bdl	bdl
FeO	0.15	0.01	0.04	0.04	0.28	0.13	bdl
MnO	bdl	bdl	0.07	0.05	0.01	bdl	bdl

MgO	bdl	bdl	bdl	bdl	bdl	bdl	bdl
CaO	54.42	53.55	54.34	54.10	53.45	54.46	53.23
Na_2O	0.54	0.07	0.03	0.09	0.08	0.03	0.07
K_2O	0.02	0.01	bdl	bdl	0.01	0.02	0.02
P_2O_5	38.10	39.91	39.92	41.05	41.14	38.99	41.12
F	5.89	5.20	4.74	4.32	4.23	5.97	5.10
Cl	0.73	0.14	0.12	0.29	0.16	0.08	0.16
Total	99.89	99.23	99.40	100.00	99.94	99.91	99.96
F/Cl	8.05	38.52	38.19	15.06	26.75	79.53	32.28

bdl = below detection limit

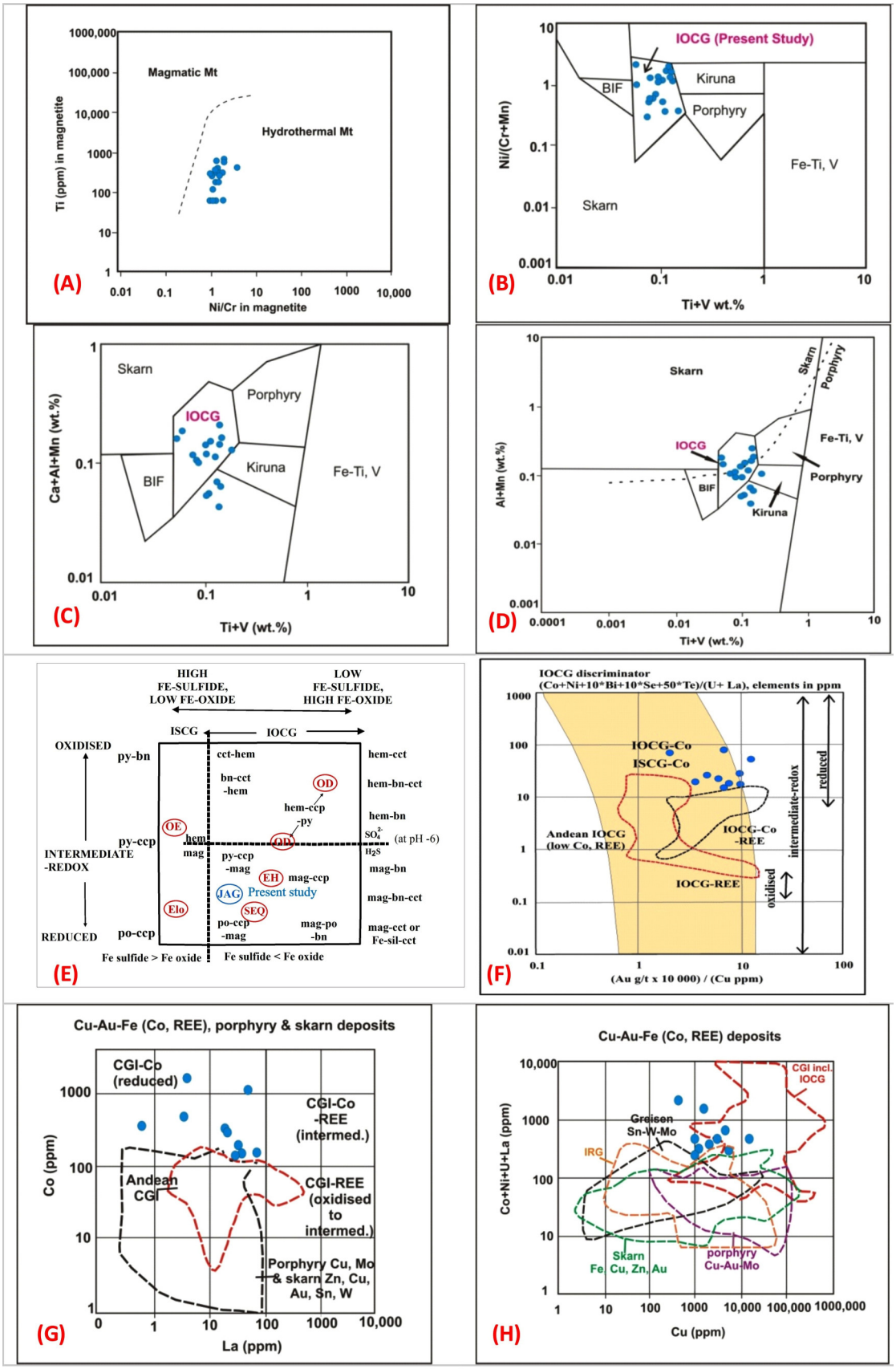

Figure 9. Trace elements plots of magnetite and geochemical discrimination diagrams suggesting IOCG type mineralization style in the study area. (**A**) Ti vs. Ni/Cr ratio of magnetite from reference [14] suggest hydrothermal nature of magnetite; (**B**) Ni/(Cr+Mn) vs. Ti+V plot from reference [18] suggesting IOCG type deposit; (**C**) Ca+Al+Mn vs. Ti+V plot from reference [18] indicates IOCG type

mineralization style; (**D**) Al+Mn vs. Ti+V plot from reference [26] also corroborate the IOCG affiliation based on magnetite EPMA data; (**E**) The IOCG-ISCG cube of the Jagpura deposit from reference[36] shows reduced mineralogical subtypes based on Fe-Cu-O-S mineral assemblages. (Key deposits are shown in red text: EH—Ernest Henry deposit, Elo—Eloise, OD—Olympic Dam, OE—Orlando East, Seq—Sequeirinho-Sossego); (**F**) The (Au g/t × 10,000)/ Cu ppm vs. (Co + Ni + 10*Bi + 10*Se + 50*Te)/(U + La) IOCG discriminator diagram for geochemical subtypes of IOCG deposit from reference[36] indicates that the Jagpura deposit is IOCG-Co (reduced) subtype; (**G**) The La vs. Co discrimination diagram from reference [36] also indicates that the Jagpura deposit is IOCG-Co (reduced) subtype and unrelated to porphyry and skarn type deposit; (**H**) The Cu vs. Co + Ni + U + La discrimination diagram from reference [36] further suggest that the Jagpura deposit is IOCG type and unrelated with porphyry Cu-Au-Mo, skarn Fe-Cu-Zn-Au, greisen Sn-W-Mo and Intrusion-Related Gold (IRG) deposits).

5.1.3. Paragenesis Study

In the Jagpura deposit, the ore minerals are semi massive to massive type, fracture fill type, vein type, disseminations/stringers type, patchy and foliation parallel types. Based on ore and gangue minerals assemblages, the texture of ore minerals and their grain boundary relationship, three different stages of ore formation are recognized (Figure 10).

Stage-I: This stage is called the dissemination/stringer stage and is characterized by fine disseminations/stringers of magnetite, arsenopyrite, pyrrhotite and chalcopyrite grains within the host rocks (Figure 7G). The common gangue mineral assemblages of this stage are quartz, biotite, apatite, albite, tourmaline, muscovite, biotite, chlorite and sericite.

Stage -II: This is the shear stage marked by the regional D_2 phase of deformation and it is the most dominant phase of mineralization in the Jagpura deposit. Most hydrothermal alterations were formed during this stage, viz. chloritization, sericitization, silicification, ferruginization and iron oxide breccia. The common gangue mineral assemblages of this stage are quartz, chlorite, sericite, biotite, apatite, albite, tourmaline and muscovite. Semi-massive to massive type ore, foliation parallel ore and vein filled ore were formed during this stage. Pyrrhotite, pyrite, chalcopyrite, magnetite, arsenopyrite, loellingite, gold, maldonite and hedleyite mineral assemblages represent the shear stage.

Stage-III: This stage is the final ore formation stage, marked by the second phase of hydrothermal fluid activity. It exhibits mineralization along fracture planes and replaces early formed ores with later ones, i.e., arsenopyrite is replaced by pyrrhotite and chalcopyrite. Native gold was precipitated in this stage, showing stringers and patchy textures.

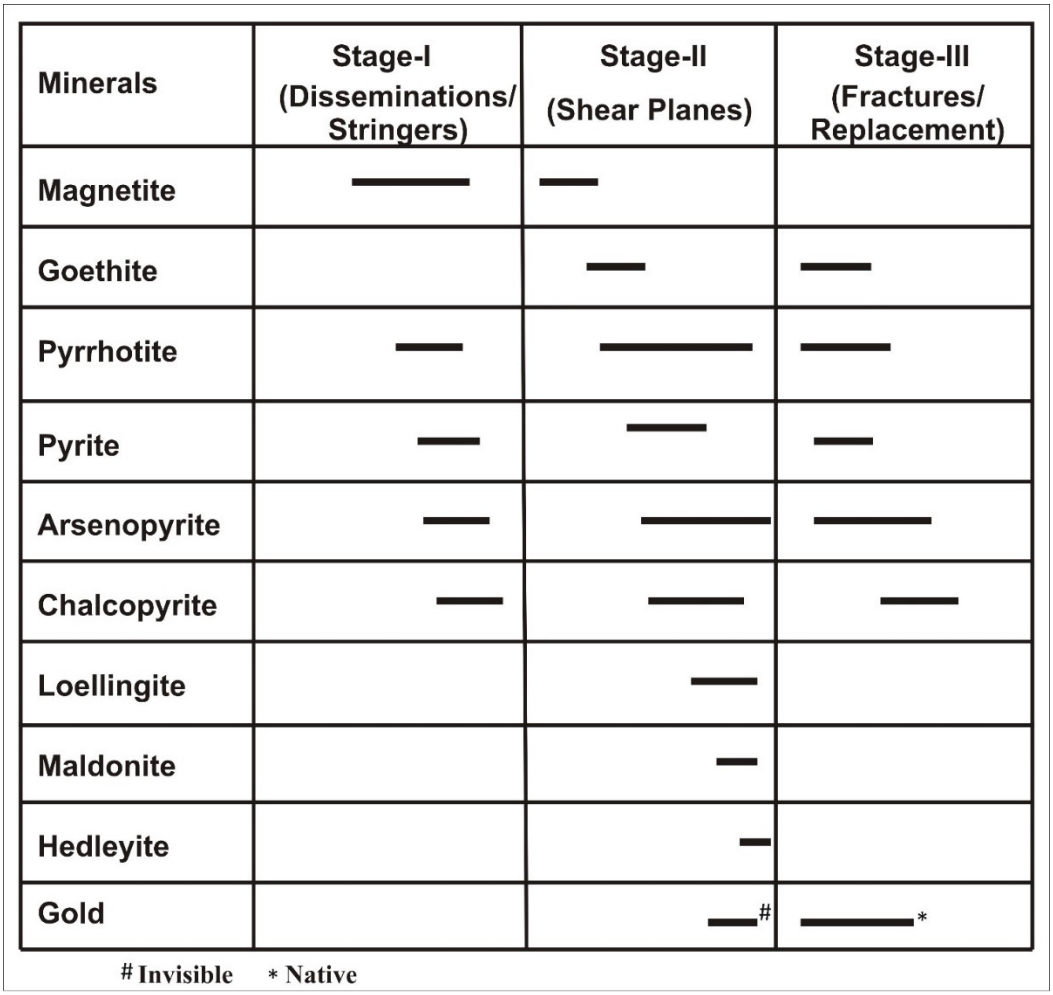

Figure 10. Paragenetic sequence showing evolution of gold mineralization with respect to various oxide and sulfide minerals based on relationships between host rock mineral assemblages, ore textural and micro-structural relationships.

5.2. Fluid Inclusion Study

5.2.1. Fluid Inclusion Petrography

Fluid inclusions were investigated using fluid inclusion assemblage (FIA) methods [66]. The size of the inclusions varies from 2 to 30 μm. The size of water vapor/CO_2 bubbles varies from 0.50 to 6.85 μm. These inclusions are classified into four types based on the phases present: type-I primary monophase carbonic inclusions, type-II primary aqueous carbonic inclusions, type-III primary aqueous bi-phase inclusions, and type-IV secondary aqueous inclusions (Figure 11).Type-I inclusions are more common and abundant in mineralized quartz veins than any other type of inclusion. These inclusions have only one phase, but two phases have been observed at room temperature in some cases. The CO_2 vapor phase is perfectly circular, spherical, and occasionally oval in shape, and at room temperature, a few of the CO_2vapor bubbles have a dark rim on the periphery due to the presence of a thin film of liquid CO_2 over vapor CO_2 and are homogenized into the liquid phase. Type-II inclusions are less common and appear in isolated patterns containing CO_2 (liquid) + CO_2 (gas) + H_2O (liquid) + NaCl. Aqueous carbonic inclusions frequently have varying degrees of fill. In general, the vapor content ranges from 25% to 60% by volume. Type-III inclusions are more abundant than any other type of inclusion, and they occur as isolated inclusions and fluid inclusion assemblages (FIA). These are usually tiny, rounded, and irregular, with two phases: liquid (H_2O+NaCl) and a vapor bubble H_2O homogenized

to liquid upon heating. The type-IV inclusions are secondary aqueous inclusions and are very similar to the aqueous inclusions of type-III.

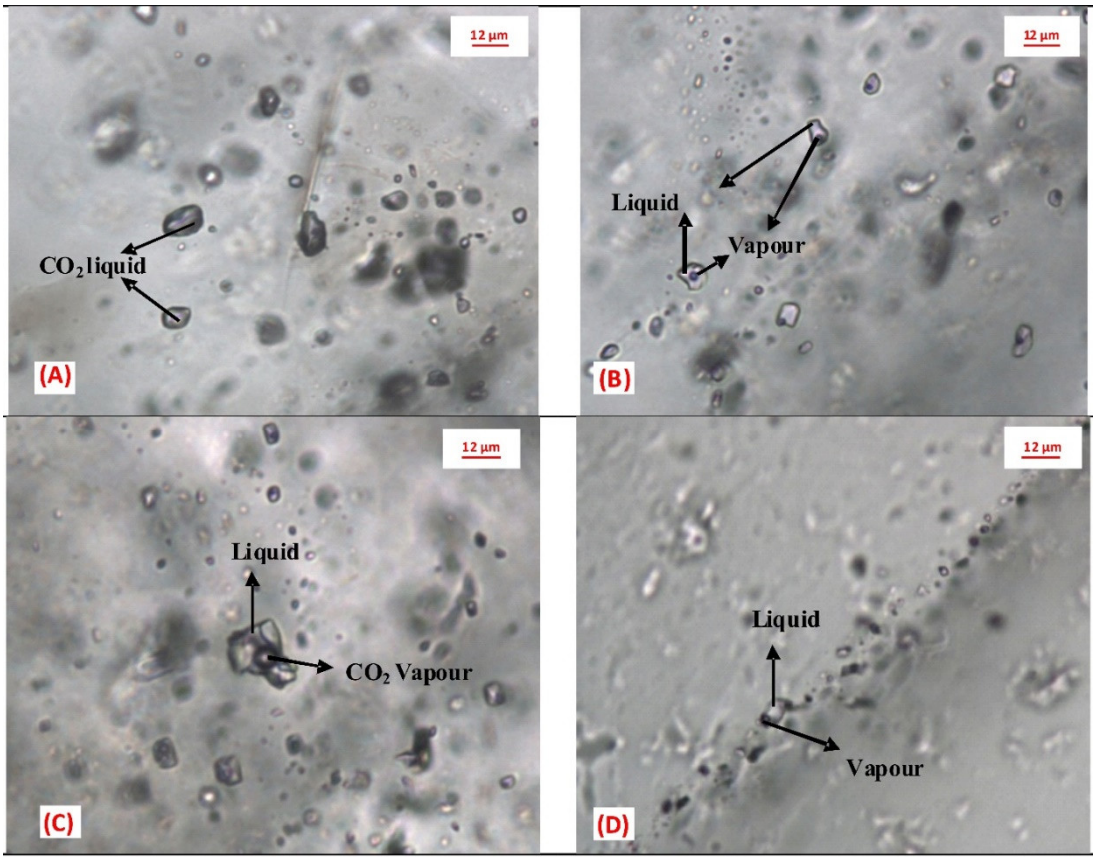

Figure 11. Types of fluid inclusions observed from study area. (**A**) Primary monophase carbonic (CO_2) inclusions; (**B**) Primary aqueous carbonic inclusions; (**C**) Primary aqueous bi-phase inclusions; (**D**) Secondary aqueous bi-phase inclusions.

5.2.2. Microthermometry

The melting temperatures (T_mCO_2) of type-I inclusions range from −56.6 to −60.2 °C, with the maximum depression in $TmCO_2$ (−60.2 °C) indicating an admixture of other gases, most likely CH_4 or N_2 [67], and the melting temperatures (Tm, CO_2) are graphically illustrated in histograms. The temperatures at which CO_2 was homogenized into the vapor phase ranged from 1.9 to 28.0 °C (density varies from 0.72 to 0.81 g/cm^3) and were graphically plotted in a histogram. The primary aqueous carbonic inclusions (type II) are less abundant and occur in isolated and cluster patterns. These are identified by the formation of vapor bubbles upon cooling, which corresponds to the composition CO_2 (liquid) + CO_2 (gas) + H_2O (liquid) + NaCl. These aqueous carbonic inclusions frequently have varying degrees of fill and coexist with aqueous-rich inclusions, inferring that fluid immiscibility occurred later in the crystallization process [66]. The total homogenization temperature (Th_{total}) ranges from 235 to 258 °C. The CO_2clathrate temperature (Tm_{clath}) ranges from 6 to 12 °C. The initial eutectic temperatures (T_e) of ice melting range from −26.5 °C to −32.0 °C. This implies that the fluid system's main component in the aqueous phase is NaCl ± $MgCl_2$. The melting temperatures of solid CO_2 range from −56.6 °C to 58.2 °C. The maximum melting temperature indicates a lesser amount of methane [68] and the homogenization temperature of CO_2 varies from 2.5 to 4.2 °C. The density of aqueous the carbonic phase varies from 0.87 to 0.98 g/cm^3. Type-III inclusions are aqueous inclusions that freeze at temperatures ranging from −52 to −72 °C. The homogenization temperature ranged from 146 to 252 °C, and the first melting (eutectic) temperatures (*Te*u) observed during the heating runs ranged from −51 to −30 °C, with an average of −41.65 °C, indicating that the

major component in the fluid system is NaCl ± $FeCl_2$. The presence of $CaCl_2$ ± $FeCl_2$ with NaCl and H_2O may be indicated by the maximum eutectic temperature of −51 °C [69]. The final melting temperature of ice (*T*m, ice) ranges from −6.9 to −30.0 °C, with salinities ranging from 10.35 to 28.15 wt% NaCl equivalent. The density of the aqueous phase varies from 0.98 to 1.10 gms/cm^3. The type-IV, secondary bi-phase inclusions are predominantly aqueous-rich. The first melting temperature (eutectic) varies from −22.5 to −44 °C with an average value of −32.1°C. This suggests that the major component in the aqueous phase is $MgCl_2$ in the fluid system. The final ice melting temperatures range from −4.5 to −22.7 °C, corresponding to the wide range of salinity varying from 7.10 to 24.09 wt% NaCl equivalents. The total homogenization temperature (Th) varies from 120 to 238 °C. The density of inclusions varies from 0.93 to 1.11 gm/cm^3 (Figure 12), [Table 4].

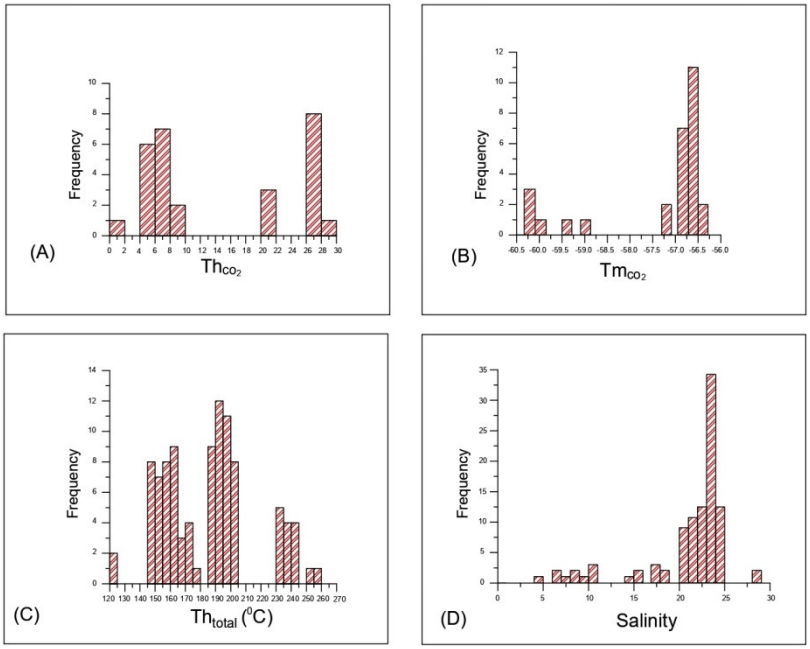

Figure 12. Histograms showing the relationship between: (**A**) Melting temperature of CO_2 ($Tmco_2$) vs. frequency; (**B**) Homogenization temperature of CO_2 ($Thco_2$) vs. frequency; (**C**) Homogenization temperature (Th_{total}) vs. Frequency; (**D**) Salinity (wt% NaCl equivalent) of the inclusion vs. frequency.

Table 4. Fluid inclusion results of different inclusions from the Jagpura deposit.

Samples	Descriptions	Type	Origin	Size (μm)	$TmCO_2$	Te	Tmice	$ThCO_2$	Th Total	Salinity	Density
Mineralized Quartz veins	Mono phase carbonic inclusions	I	Primary	2–15	−56.6 to −60.2°C	-	-	1.9 to 28°C	-	-	0.66 to 0.92 g/cc
	Aqueous carbonic inclusions	II	Primary	6–30	−56.6 to 58.8 °C	−26.5 to −32°C	−3 to −7°C	2.5 to 4.2 °C	235 to 258 °C	4.86 to 10.48	0.87 to 0.98 g/cc
	Aqueous inclusion	III	Primary	2–28		−30 to −51°C	−6.9 to −30.0°C	-	146 to 252°C	10.35 to 28.15	0.98 to 1.10 g/cc
	Secondary aqueous inclusions	IV	Secondary	1–15		−22.5 to −44°C	−4.5°C to −22.7°C	-	120 to 238°C	7.10 to 24.09	0.93 to 1.11 g/cc

5.3. Sulfur Isotopic Composition

The $\delta^{34}S_{VCDT}$ (‰) values obtained from major sulfide minerals of the Jagpura deposit show a narrow range from +08.89 to +14.58‰ with an average value of +11.16‰ [Table 5]. The $\delta^{34}S$ value of pyrite ranges from 10.28 to 11.05‰, pyrrhotite from 8.89to 12.34‰, chalcopyrite from 10.14to 12.14‰ and arsenopyrite from 10.98 to 14.58‰. The average $\delta^{34}S$ values of pyrite, pyrrhotite, chalcopyrite and arsenopyrite are +10.60‰, +10.65‰, +11.15‰ and +12.31‰, respectively, in the increasing order of heavier isotope enrichment of $\delta^{34}S$ values.

Table 5. $\delta^{34}S_{VCDT}$ (‰) values of various sulfide minerals of the Jagpura deposit.

Sl. No.	Sample No.	$\delta^{34}S$ VCDT‰	St. dev.	Sulfide Mineral Phase
1.	JPSI-1	8.89	0.20	Pyrrhotite
2.	JPSI-2	9.80	0.17	
3.	JPSI-3	10.87	0.37	
4.	JPSI-4	10.67	0.16	
5.	JPSI-5	10.52	0.27	
6.	JPSI-6	10.82	0.31	
7.	JPSI-7	11.36	0.14	
8.	JPSI-8	12.34	0.37	
9.	JPSI-9	12.81	0.11	Arsenopyrite
10.	JPSI-10	10.98	0.20	
11.	JPSI-11	11.00	0.07	
12.	JPSI-12	11.42	0.13	
13.	JPSI-13	11.73	0.16	
14.	JPSI-14	13.68	0.11	
15.	JPSI-15	14.58	0.08	
16.	JPSI-16	10.77	0.10	Chalcopyrite
17.	JPSI-17	10.90	0.05	
18.	JPSI-18	11.18	0.26	
19.	JPSI-19	10.99	0.03	
20.	JPSI-20	10.14	0.09	
21.	JPSI-21	10.67	0.33	
22.	JPSI-22	11.56	0.18	
23.	JPSI-23	12.03	0.28	
24.	JPSI-24	12.14	0.15	
25.	JPSI-25	10.28	0.06	Pyrite
26.	JPSI-26	10.39	0.16	
27.	JPSI-27	10.29	0.05	
28.	JPSI-28	10.71	0.46	
29.	JPSI-29	11.05	0.52	
30.	JPSI-30	10.62	0.30	
31.	JPSI-31	10.87	0.59	

5.4. Geochemical Results

The values of Fe in oxide range from 11.25 to 42.22 wt% and values of Fe in sulfide range from 4.27 to 22.37 wt%. The value of nickel ranges from 70 to 400 ppm, cobalt from 130 to 1600 ppm, Cu from 470 to 15,200 ppm, Cr from 155 to 348 ppm, Au from 0.20 to 18.60 ppm, Pb from 25 to 400 ppm, Zn from 10 to 100 ppm, La from 0.64 to 75.61 ppm and U from 2.42 to 3.84 ppm [Table 6]. The total REE varies from 76.64 to 346.38 ppm. The

geochemical result shows enrichment of Co, Ni in Cu-Au ores and low values of REE and U.

Table 6. Geochemical results of samples from theJagpura deposit.

Lithology: Quartz-Mica Schist										
Trace Elements & REEs (ppm)										
Ga	38	31	28	54	69	46	53	46	51	109
Sc	10	11	10	23	20	09	09	9	13	11
V	78	85	92	122	90	104	87	88	92	88
Th	20	21	30	27	26	30	23	21	27	22
Pb	120	400	70	40	50	30	25	25	25	40
Ni	300	140	100	90	130	70	80	100	70	400
Co	1100	950	480	860	480	730	290	330	840	1600
Cr	155	176	179	306	348	223	234	215	218	228
Sr	69	70	72	78	64	56	63	68	68	53
Zr	142	134	121	97	76	119	102	105	114	60
Cu	4600	2400	1200	15200	4700	4600	3100	7100	1100	4700
Zn	20	100	10	40	20	20	10	10	10	10
Be	3.88	4.30	3.47	2.67	2.94	3.00	2.34	1.82	2.48	1.54
Ge	1.64	1.72	1.52	1.03	0.98	1.32	1.23	1.31	1.42	1.11
Y	34.86	28.68	19.68	47.61	96.01	23.40	19.14	19.99	18.95	38.82
Mo	1.54	1.74	2.10	2.38	4.23	2.28	3.29	3.00	2.88	3.00
Sn	3.76	3.76	3.73	3.81	2.74	3.98	2.75	3.21	3.76	5.06
La	50.29	75.60	34.52	10.63	32.64	31.74	21.73	19.90	16.53	24.16
Ce	89.24	133.66	59.79	0.06	4.93	56.72	39.25	35.17	65.10	6.87
Pr	10.41	15.44	6.99	0.27	0.86	6.79	4.96	4.37	7.83	1.02
Nd	40.40	59.37	28.11	1.72	4.35	27.60	19.83	17.54	31.42	4.74
Sm	6.88	9.26	4.73	0.86	1.67	4.31	3.53	2.78	5.05	1.21
Eu	1.24	1.62	0.84	0.34	0.49	0.89	0.75	0.66	0.95	0.41
Gd	6.32	7.62	4.04	2.71	5.40	3.85	3.25	2.84	4.17	2.34
Tb	1.18	1.27	0.73	1.00	1.98	0.74	0.62	0.58	0.69	0.77
Dy	7.05	6.15	4.07	8.34	17.44	4.61	3.60	3.63	3.78	6.74
Ho	1.31	1.11	0.74	1.76	3.60	0.89	0.72	0.76	0.68	1.39
Er	3.72	3.09	2.23	4.84	9.88	2.61	2.01	2.17	2.00	3.91
Tm	0.58	0.45	0.31	0.71	1.40	0.37	0.28	0.31	0.27	0.56
Yb	3.39	2.65	2.04	3.93	7.50	2.42	1.74	2.02	1.82	3.26
Lu	0.46	0.38	0.30	0.52	0.95	0.31	0.25	0.29	0.26	0.45
Hf	4.36	4.20	4.15	3.27	2.83	4.61	3.80	3.88	3.89	2.82
Ta	1.27	1.14	1.16	1.46	0.66	1.26	1.14	1.11	1.06	0.88
W	27.00	6.42	6.47	6.76	4.76	14.72	11.26	11.41	11.70	10.11
U	3.15	3.31	2.42	3.62	2.98	3.83	3.48	3.39	3.16	2.89
Bi	0.16	0.27	0.38	2.65	2.94	1.31	2.17	2.33	1.05	5.46
Te	1.26	1.09	1.02	0.20	0.27	1.21	0.97	0.92	1.02	1.01
Se	0.20	0.20	0.20	0.20	0.20	0.20	0.20	0.20	0.20	0.20
Au	4.62	1.70	1.20	3.10	1.70	2.20	2.40	4.30	1.40	3.30

6. Discussion

6.1. Nature and Control of Mineralization

The mode of occurrence of mineralization as (1) semi-massive to massive type, (2) vein and fracture fill type, (3) foliation parallel disseminations/smears and (4) patchy and stringer type indicates hydrothermal origin of the mineralizing fluid. Textural investigations indicate the mineralization occurring as a fracture and open space-filling. The mineral boundary relationship, exsolution and the replacement and deformation textures further substantiate the hydrothermal nature of mineralization. This is further corroborated by the presence of iron oxide breccia, epigenetic quartz and pegmatite veins within the deposit. The ore mineralization is associated with pervasive hydrothermal Na-B alteration besides Fe-Mg-Ca-K alteration. Disseminated mineralization occurs parallel to S_0 II S_1 planes, related to the first deformation episodes. The ore mineralization is remobilized and concentrated within the hinge zone of F_2 folds and sympathetic shears (Figures 6E,F and 7F,H) during second phase of deformation. The NW-SE trending shear planes are parallel to F_2 axial planes of the second stage deformation event. The ore localization along these structures suggests distinct structural control of mineralization in the study area.

6.2. Geochemistry of Native gold, Pyrite, Magnetite, Apatite and Their Implications

EPMA analysis of gold indicates that Au concentration ranges from 89.25 to 94.72 wt% and it contains silver as minor impurity (6.15 to 8.46 wt%). Gold fineness ranges between 914–937‰ with an average value of 927‰ indicating high purity gold. The Co/Ni ratio of pyrite is >1 (1 to 2.54) suggests hydrothermal origin [64,69–71], [Table 1; Figure 8G].

The Co/Ni ratios [15], Ti and V concentrations [14,72,73] are important parameters to differentiate hydrothermal magnetite to magmatic magnetite. The hydrothermal magnetite is depleted in Ti (<2 wt%) and Al (<1 wt%), [14,15,18,20,26,74]. Low TiO_2 (0.01 to 0.11 wt%) and Al_2O_3 (0.06 to 0.28 wt%) concentrations in magnetite indicates the presence of hydrothermal magnetite in the study area [Table 2]. The Ti vs. Al and Ti vs. Ni/Cr bivariate plot of magnetite from study area also indicates magnetite is hydrothermal in origin (Figures 8H and 9A). The Ni/(Cr + Mn) vs. Ti + V plot, Ca + Al + Mn vs. Ti + V and Al + Mn vs. Ti + V plot of magnetite suggest IOCG deposit style (Figure 9B–D). Apatite from study area is of fluorapatite variety with F content >1 wt% (4.23 to 5.97 wt%) and >1 F/Cl ratio [Table 3]. Apatite has a higher concentration of F and a lower concentration of Cl, FeO, and MnO, which indicate that it is hydrothermal in nature and is sourced from metavolcano-sedimentary units [75].

6.3. Evolution of Ore Fluids

The characteristics of the mineralized quartz vein hosted fluid inclusions are listed in Table 4 and Figures 10 and 11. The homogenization temperature versus salinity diagram indicates that the mineralization within the Jagpura Au-Cu deposit is the result of the isothermal mixing of ore fluids with boiling/effervescence (Figure 13A), [76]. Most hydrothermal deposits have coexisting liquid rich, highly saline, and vapur rich low saline inclusions, indicating that the different phases are generated by immiscibility [77].

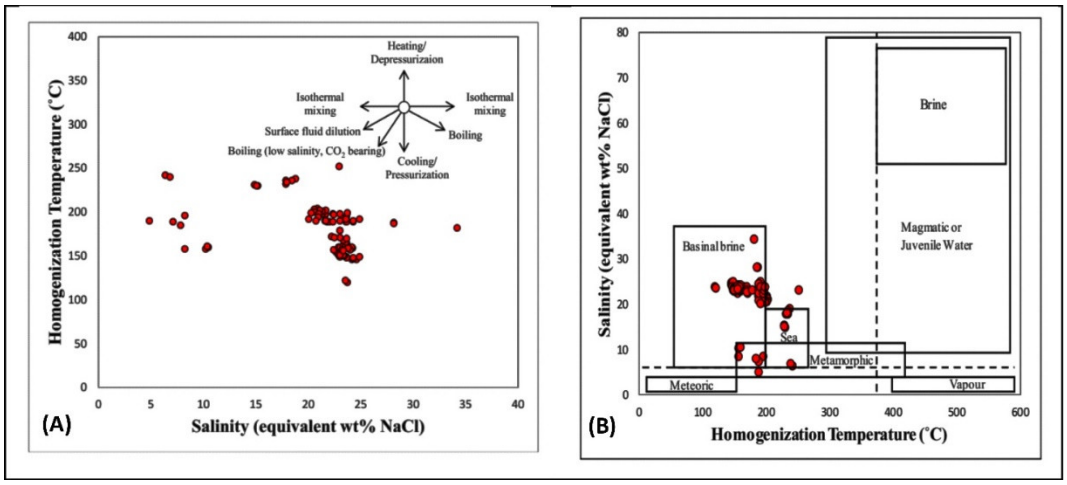

Figure 13. Homogenization temperature vs. salinity diagram of fluid inclusions from study area:(**A**) showing typical trends in homogenization temperature-salinity space due to various fluid evolution processes, from reference [78]; (**B**) Salinity vs. Homogenization temperature diagram from reference [79] indicates mixing of basinal brine, sea water and metamorphic fluids in ore fluid.

In the study area, type-III inclusions are liquid rich [(H_2O + NaCl (l)] and highly saline (10.35–28.15 wt% NaCl equivalent); however, type-II inclusions are vapor rich and low saline (4.8–10.48 wt% NaCl equivalent). These data indicate that there is an immiscibility of ore fluids. Generally, salinity of metamorphic fluids ranges between 3–10 wt% NaCl, with homogenization temperature varying between 150–425 °C and salinity of the basinal brine ranges between 5–40 wt% NaCl, with low homogenization temperature varying between 75–200 °C. In the Jagpura area, type-II inclusions match with the metamorphic fluids whereas type-III inclusions show similar character with basinal brine. Salinity versus homogenization temperature diagram indicates that the ore fluid is the result of the mixing of basinal brine, sea water and metamorphic fluids (Figure 13B), [80]. The high saline ore fluid transported metals in the system as metals chloride complex.

6.4. Source of Metals, Sulfur and Ore-Forming Fluids

The $\delta^{34}S_{VCDT}$ values of sulfides from the Jagpura Au-Cu deposit are within the range of 8.98- to 14.58‰, with an average value of 11.16‰ (Figure 14A). This narrow range of sulfur isotopes indicates that (i) sulfur has originated from one uniform source under stable physicochemical condition or (ii) local disequilibrium between two phases of mineralization [81].

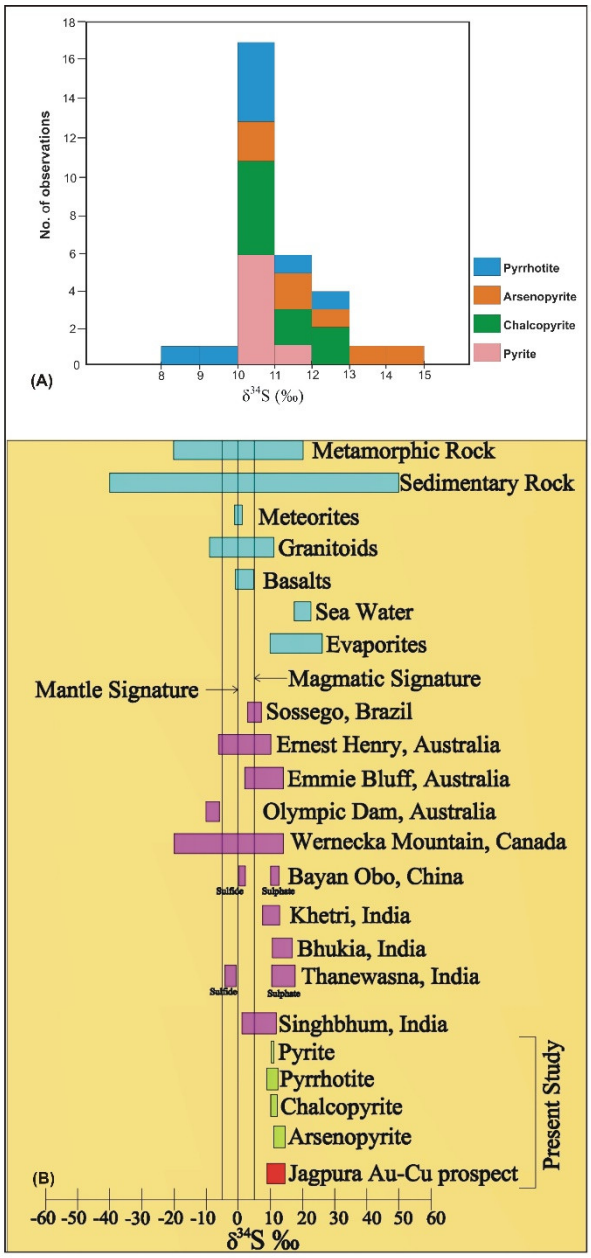

Figure 14. Sulfur isotope compositions of different sulfide minerals from the Jagpura deposit: (**A**) Histogram showing values of various sulfide minerals; (**B**) Range of $\delta^{34}S$ for magmatic, sedimentary, metamorphic, seawater and evaporite systems from references [59,82]. Plot showing the variation in $\delta^{34}S$ values of sulfides from the Jagpura IOCG deposit, and comparison of the $\delta^{34}S$ values of sulfides from the Jagpura deposit with major geological sulfur reservoir and with various IOCG deposit worldwide from reference [24,83] and India from references [27,28,31,39,44,84].

The major gold bearing sulfide mineral within the Jagpura Au-Cu deposit is arsenopyrite and it contains a higher isotopic ratio than the other sulfide phases. The higher isotopic range in the sulfur isotope compositions imply that sulfide minerals are enriched in heavy isotopes (Figure 14B). In various deposits around the world, isotopically heavy sulfur ($\delta^{34}S > 5$) suggests the presence of non-magmatic sulfur sources. Higher positive values of the sulfur isotope rule out magmatic ($\delta^{34}S = 05$), [85,86], mantle ($\delta^{34}S = 01$), [87], and seawater/biogenic sulfur sources ($\delta^{34}S = > 20$), [83]. The presence of relatively higher $\delta^{34}S$ rich sulfides indicates that the possible source of heavy sulfurs is (i) seawater, (ii) evaporitic water and (iii) oxidized meta-sedimentary fluids [88,89]. Therefore, the

moderately high $\delta^{34}S$ values of the Jagpura deposit values suggest a meta-sedimentary source for sulfur.

The lack of sulfate minerals in the Jagpura deposit indicates that the sulfur was present in the hydrothermal fluids as reduced sulfur (H_2S). The potential source of reduced H_2S was the basement rocks. The sulfur isotope compositions of sulfides from the Jagpura deposit are similar to the major geological sulfur reservoirs and other IOCG type deposits in India and the world (Figure 14B). External fluids, primarily basinal brines and modified seawater with high $\delta^{34}S$values (>+10), play an important role in IOCG ore-forming systems [90]. The sulfur isotope data indicate the mixed source of sulfur derived from the non-magmatic hydrothermal fluids, and the high saline brine (marine/evaporitic). Variation in the sulfur isotopic compositions of sulfides is the result of dilution and cooling of the metalliferous fluid derived from the basement meta-sedimentary rocks, which along with highly saline brine triggered the precipitation of Au along structural weak planes.

6.5. Geochemical Characterization of the Jagpura Deposit

There are three mineralogical subtypes of IOCG deposits based on dominant ore assemblages i.e., (i) oxidized (ii) intermediate-redox and (iii) reduced mineralogical subtypes [36]. The reduced mineralogical subtypes are represented by pyrrhotite and/or Fe-silicates and variable modal proportions of magnetite, pyrite, and chalcopyrite. The reduced IOCG-ISCG deposit group commonly includes phases hosting Co, Ni, As and Bi; however, REE, U, fluorite, barite or anhydrite phases are rare [36]. The Jagpura deposit is represented by the dominant ore assemblages of pyrrhotite-chalcopyrite-arsenopyrite-pyrite-magnetite. The deposit includes phases hosting Co, Ni, As and Bi; however, REE, U, fluorite and barite are not present. The IOCG-ISCG cube diagram based on Fe-Cu-O-S mineral assemblages (Figure 9E) suggests that the Jagpura deposit is characterized by reduced mineralogical subtypes. The geochemical result shows enrichment of Co, Ni in Cu-Au ores and low values of REE and U [Table 6]. The occurrence of >15% Fe in oxide, (Au g/t× 10,000)/ Cu ppm vs. (Co + Ni + 10*Bi + 10*Se + 50*Te)/(U + La), La vs. Co and Cu vs. Co+Ni+U+La geochemical discrimination diagrams (Figures 9F–H) for geochemical subtypes of Cu-Au-Fe (± Co, REE) deposits including IOCG deposits indicates that the Jagpura is IOCG-Co (reduced) subtype deposit and unrelated to porphyry Cu-Au-Mo, skarn Fe-Cu-Zn-Au, greisen Sn-W-Mo, and intrusion-related gold (IRG) deposits.

6.6. Genesis of the Jagpura Au-Cu Deposit

The genesis of an ore deposits is closely related to the geological environments, i.e., pressure -temperature conditions, and the nature/source of the hydrothermal fluids [66,73,78,79]. Fluid inclusion study is a vital tool to understand the genetic aspects, whereas the sulfur isotope signatures help in the understanding of the nature and source of the mineralizing fluids of an ore deposit. [90–92]. Sulfur isotope data also provides the information about the source of metals in a deposit [59,93]. The sulfur isotope variations in an ore mineralizing systems are very complex and, hence, best understood in the context of the total geological framework of a deposit in conjunction with the fluid inclusion study.

Au-Cu sulfide mineralization within the Jagpura deposit is hosted by quartz-mica schist and albitite. The mineralization is localized along NW-SE trending D_2 shear planes parallel to F_2 axial planes and F_2 fold hinges and correlated to the second deformation phase (Figure 15). The ore mineral association is represented by the iron oxide (magnetite), copper, gold and apatite. The mineralization includes arsenopyrite, loellingite, chalcopyrite, pyrrhotite and pyrite, along with the native gold and abundant magnetite. Further the maldonite and hedleyite occur as Au-Bi-Te phases. The mode of occurrence of mineralization as open space-filling, vein and fracture fill type indicates hydrothermal nature. The mineralization is associated with pervasive hydrothermal Na-B alteration besides Fe-Mg-Ca-K alteration. The occurrence of maldonite, hedleyite associated with gold lode,

epigenetic quartz-pegmatite veins in host rocks and pervasive hydrothermal alteration indicate hydrothermal origin of ore fluids.

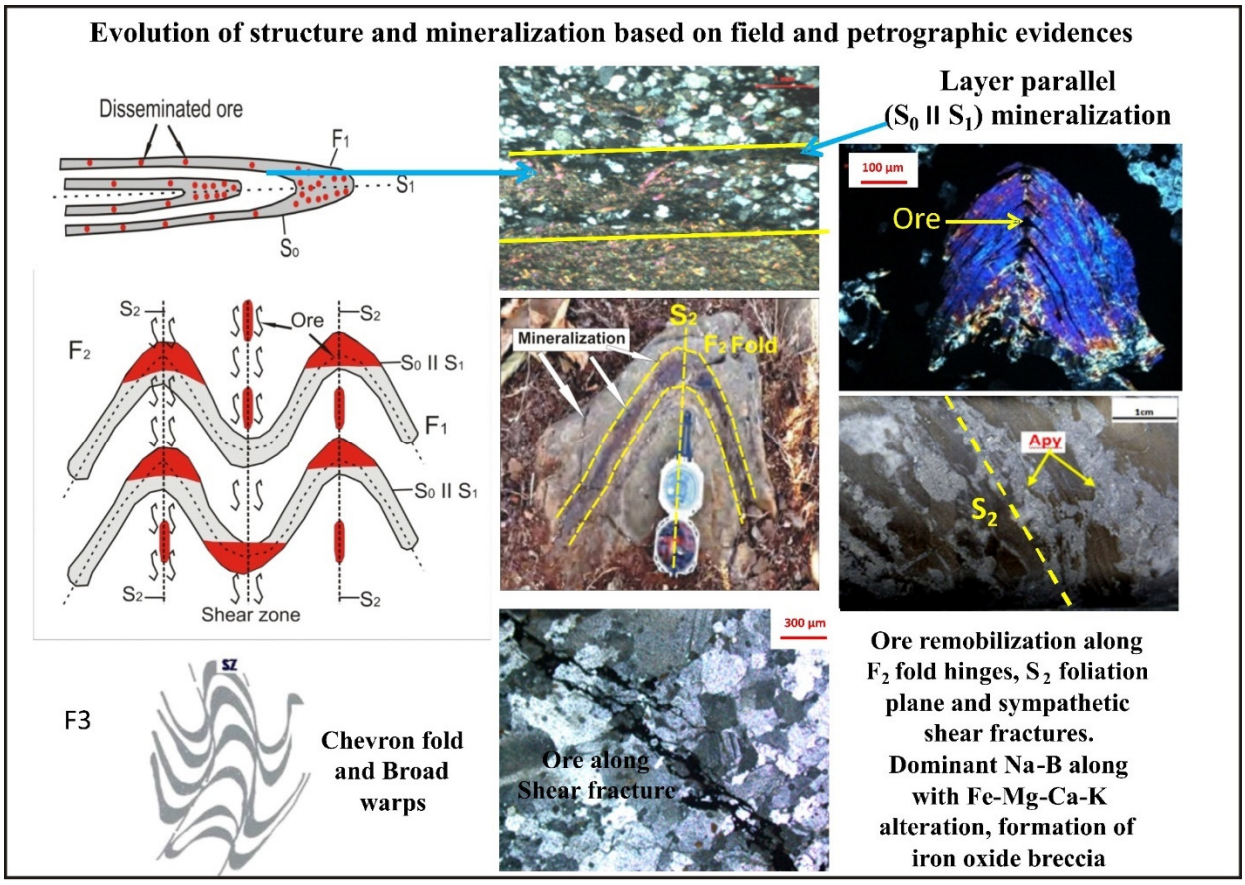

Figure 15. Schematic diagram showing the stage of evolution of the structure and polymetallic mineralization at theJagpura deposit based on field and petrographic studies.

The Co/Ni ratio of >1 in pyrite, gold-sulfide associated low TiO_2, Al_2O_3 hydrothermal magnetite (Co/Ni ratio < 1 and Ni/Cr ≥ 1) and fluorapatite (>1 F/Cl ratio) support the hydrothermal origin of mineralization. Apatite has a higher F concentration and a lower concentration of Cl, FeO, and MnO, indicating its source from the metavolcano-sedimentary units. Fluid inclusions micro-thermometry indicates the presence of aqueous rich, mixed carbonic-aqueous and minor vapor rich aqueous inclusions. The FI's show episode of fluid immiscibility with the homogenization temperatures and salinities varying between 120–258 °C and 8.86–28.15 wt% NaCl eq., respectively. This data indicates that the high saline ore fluids are injected during the D_2 phase of deformation. The high salinity ore fluid transport metals in the ore system as metals chloride complex.

The iron oxide-copper-gold (IOCG) type deposits are characterized by abundant (>10%) hydrothermal iron oxides (magnetite or hematite) and economic grade Cu and/or Au. It also contains Ag, U, Th, F, Co, Bi, W, rare earth elements (REE) and other metals. These deposits are diverse in age (Neo-Archaean to the Cenozoic), tectonic setting, P–T conditions, characteristic Na-Ca-K alterations, host-rock package and mineralization style [36,90,94–98].The field characteristics, trace element geochemistry of pyrite, apatite and magnetite, fluid inclusion and sulfur isotope compositions of the Jagpura Au-Cu deposit are compared with the Epithermal gold deposit of high sulfidation and low sulfidation, Carlin type gold deposit, Orogenic lode gold and IOCG type Cu-Au deposits [4–10] and this suggeststhat the Jagpura gold-copper ore system is similar to the IOCG type. The Jagpura Au-Cu deposit indicate the: (i) iron oxide-copper-gold-apatite association of hydrothermal origin, (ii) distinct structural control of mineralization, (iii) Na-B-Mg-Fe-Ca-K

hydrothermal alteration(dominant Na-B alteration), (iv) presence of iron oxide breccia, (v) abundant hydrothermal Fe oxides (>15%), (vi) trace element geochemistry of magnetite (Ti, Al + Mn, Ti + V concentrations and Ni/(Cr + Mn) vs. Ti + V, Ca + Al + Mn vs. Ti + V, Al + Mn vs. Ti + V ratios of magnetite Figures 8J–L) suggests IOCG style of mineralization, (vii) presence of late-stage sulfides with economic gold-copper resources, (viii) high saline ore fluid and sulfur isotope compositions within the range of IOCG deposits worldwide (−30 to +26‰) and (ix) The (Au g/t × 10,000)/ Cu ppm vs. (Co + Ni + 10*Bi + 10*Se + 50*Te)/(U + La), La vs. Co and Cu vs. Co + Ni + U + La and discrimination diagrams (Figure 9F–H), [36] indicates a IOCG-Co (reduced) subtype deposit and is unrelated to porphyry Cu-Au-Mo, skarn Fe-Cu-Zn-Au, greisen Sn-W-Mo, and intrusion-related gold (IRG) deposits. These characters of the Jagpura deposit are well corroborated with the IOCG-IOA type and the IOCG-Co (reduced) subtype deposit.

7. Conclusions

The Jagpura Au-Cu deposit shows pervasive hydrothermal alteration zones associated with the iron-oxide and sulfide mineralization along the brittle-ductile shear zone. The ore petrography and EPMA study show the presence of Au-Bi-Te phases, Co/Ni ratio of >1 in pyrite, gold-sulfide associated low TiO_2, Al_2O_3 hydrothermal magnetite (≥1 Ni/Cr ratio, <1 Co/Ni ratio). The presence of apatite with higher F concentration (>1 F/Cl ratio) and a lower concentration of Cl, FeO and MnO is consistent with its hydrothermal origin. Fluid inclusion microthermometric studies indicate the presence of aqueous rich, mixed carbonic-aqueous and minor vapor rich aqueous inclusions. The FI's show episodes of fluid immiscibility with the homogenization temperatures and salinities range of 120–258 °C and 8.86–28.15 wt% NaCl eq., respectively. These data indicate a mixture of highly saline ore fluid of basinal brine and metamorphic origin, responsible for the transport of metals in the system as metals chloride complex. The $\delta^{34}S$ values of sulfides are within a narrow range of 8.98‰ to 14.58‰, with an average value of 11.16‰. This indicates the non-magmatic origin of sulfides. Variation in the sulfur isotopic compositions of sulfides resulted from the dilution and cooling of the metalliferous fluid derived from the basement rocks. The mixing of high saline brine triggered the gold precipitation along the structural discontinuities. The Ti, Al + Mn, Ti + V concentrations and Ni/(Cr + Mn) vs. Ti + V, Ca + Al + Mn vs. Ti + V, Al + Mn vs. Ti + Vratios of magnetite suggest an IOCG type of mineralization. The (Au g/t × 10,000)/ Cu ppm vs. (Co + Ni + 10*Bi + 10*Se + 50*Te)/(U + La), La vs. Co and Cu vs. Co + Ni + U + La geochemical discrimination diagrams indicates that the Jagpura Au-Cu deposit is an IOCG-Co (reduced) subtype deposit. Iron oxide-copper-gold-apatite association of hydrothermal origin, nature and distinct structural control of mineralization, pervasive hydrothermal alteration, trace element characteristics of magnetite, pyrite and apatite, high saline ore fluid and sulfur isotope compositions suggest that the Jagpura deposit is an IOCG-IOA type and is similar to those described for the shear fault-controlled-IOCG deposits found elsewhere in the world. The classification of the Jagpura deposit as an IOCG-IOA type: IOCG-Co (reduced) subtype has significant implications for the deeper level sub-surface exploration in the Salumber Ghatol Metallogenic Belt within the Aravalli Craton.

Author Contributions: Conceptualization, A.A., S.S.; methodology, A.A., S.S., A.G.; validation, S.S., A.A., A.G..; investigation, A.A., A.S., M.K.; writing original draft preparation, A.A., A.G., M.K., G.K.M.; writing, review and editing, S.S., A.S.; visualization, A.A., A.G.; Formal analysis, A.A., G.K.M., M.K.; supervision, S.S., A.S. All authors have read and agreed to the published version of the manuscript.

Funding: This study is supported by the Geological Survey of India, Western Region, Jaipur.

Institutional Review Board Statement: Not applicable.

Informed Consent Statement: Not applicable.

Data Availability Statement: The data presented in this study are mainly contained within the article and available in the references listed. To a minor degree, the data presented are not publicly available due to privacy and available on request from the first author.

Acknowledgments: The authors are extremely grateful to S. Raju, Director General, Geological Survey of India (GSI), Kolkata, Shri Jaya Lal, Addl. Director General &HoD, Western Region (WR), Jaipur and Sanjay Das, Deputy Director General, State Unit, Rajasthan, GSI, WR, Jaipur for their continuous encouragement and permission to publish this paper. AA extends sincere thanks to GSI for providing an opportunity to carry out research in the Jagpura area (project no.99) and extends sincere gratitude to Shri R. L. Jat, Shri Sanjay Singh, Shri Hemant Kumar Singh and Shri Lalit Mohan, GSI for providing help and guidance during field work. AA extends sincere thanks to M. L. Dora, GSI for their valuable suggestions and help to improve this manuscript. We also acknowledge and express sincere thanks to Shri Manish M. John, IRMS Lab, GSI, Bengaluru, Smt. Sonalika Joshi, EPMA Lab, GSI, Faridabad and personnel of EPMA Lab, IIT, ISM, Dhanbad for analyzing the samples. AA thanks Mohini S. Sathe, Geologist, GSI, WR for wholehearted support and encouragement during the writing of this article. The authors also acknowledge GSI's in house reviewers for their constructive and thoughtful comments, which helped in improving the quality of the manuscript. Authors extend their sincere thanks and gratitude to the Editor-in-Chief Paul Sylvester, Special Issue Editor Galina Palyanovaandanonymous reviewers for their continuous encouragement and kind suggestions for improving the quality of the manuscript.

Conflicts of Interest: The authors declare that they have no known competing financial interest or personal relationships that could have appeared to influence the work reported in this paper. There is no conflict of interest as this work is Ph.D work of first author, due acknowledgment has been given to pervious work. Author has intimated the competent authority of Geological Survey of India (GSI) to publish this work in the said journal.

References

1. Palyanova, G.; Murzin, V.; Borovikov, A.; Karmanov, N.; Kuznetsov, S. Native Gold in the Chudnoe Au-Pd-REE Deposit (Subpolar Urals, Russia): Composition. Minerals in Intergrowth and Genesis. *Minerals* **2021**, *11*, 451. https://doi.org/10.3390/min11050451.
2. Liu, H.; Beaudoin, G. Geochemical signatures in native gold derived from Au-bearing ore deposits. *Ore Geol. Rev.* **2021**, *132*, 104066. https://doi.org/10.1016/j.oregeorev.2021.104066.
3. Savva, N.E.; Kravtsova, R.G.; Anisimova, G.S.; Palyanova, G.A. Typomorphism of Native Gold (Geological-Industrial Types of Gold Deposits in the North-East of Russia). *Minerals* **2022**, *12*, 561. https://doi.org/10.3390/min12050561.
4. Groves, D.I.; Goldfarb, R.J.; Gebre-Mariam, M.; Hagemann, S.G.; Robert, F. Orogenic gold deposits: A proposed classification in the context of their crustal distribution and relationship to other gold deposit types. *Ore Geol. Rev.* **1998**, *13*, 7–27.
5. Goldfarb, R.J.; Groves, D.I.; Gardoll, I. Orogenic gold and geologic time: A global synthesis. *Ore Geol. Rev.* **2001,** *18*, 1–75.
6. Cline, J.S.; Hofstra, A.H.; Muntean, J.L.; Tosdal, R.M.; Hickey, K.A. Carlin-type gold deposits in Nevada: Critical geologic characteristics and viable models. In *Economic Geology 100th Anniversary Volume* 2005; Society of Economic Geologists: Littleton, CO, USA, 2005; pp. 451–484.
7. Sinclair, W.D. Porphyry deposits. Mineral Deposits of Canada: A Synthesis of Major Deposit-Types, District Metallogeny, the Evolution of Geological Provinces, and Exploration Methods. In *Geological Association of Canada*, *Mineral Deposits Division*, *Special Publication*;Geological Association of Canada: St. John's, NL, Canada, 2007; Volume5, pp. 223–243.
8. Sillitoe, R.H. Porphyry copper systems. *Econ. Geol.* **2010**, *105*, 3–41.
9. Groves, D.I.; Bierlein, F.P.; Meinert, L.D.; Hitzman, M.W. Iron oxide copper-gold (IOCG) deposits through Earth history: Implications for origin, lithospheric setting, and distinction from other epigenetic iron oxide deposits. *Econ. Geol.* **2010**, *105*, 641–654.
10. Goldfarb, R.J.; Groves, D.I. Orogenic gold: Common or evolving fluid and metal sources through time. *Lithos* **2015**. https://doi.org/10.1016/j.lithos.
11. Frimmel, H.E. Earth's continental crustal gold endowment. *Earth Planet. Sci. Lett.* **2008**, *267*, 45–55.
12. Klemm, D.D.; Henckel, J.; Dehm, R.M.; Von Gruenewaldt, G. The geochemistry of titanomagnetite in magnetite layers and their host rocks of the eastern Bushveld Complex. *Econ. Geol.* **1985**, *80*, 1075–1088.
13. Nadoll, P.; Koenig, A.E. LA-ICP-MS of magnetite: Methods and reference materials. *J. Anal. At. Spectrom.* **2011**, *26*, 1872–1877.
14. Dare, S.A.S.; Barnes, S.J.; Beaudoin, G. Variation in trace element content of magnetite crystallized from a fractionating sulfide liquid, Sudbury, Canada: Implications for provenance discrimination. *Geochim. Cosmochim. Acta.* **2012**, *88*, 27–50. https://doi.org/10.1016/j.gca.2012.04.032.
15. Dare, S.A.S.; Bames, S.J.; Beaudoin, G.; Meric, J.; Boutroy, E.; Potvin-Doucet, C. Trace elements in magnetite as petrogenetic indicators. *Miner. Depos.* **2014**, *49*, 785–796. https://doi.org/10.1007/s00126-014-0529-0.

16. Huang, X.W.; Beaudoin, G. Textures and chemical composition of magnetite from iron oxide-copper-gold (IOCG) and Kiruna-type iron oxide-apatite (IOA) deposits and their implications for ore genesis and magnetite classification schemes. *Econ. Geol.* **2019**, *114*, 953–979.
17. Carew, M.J.; Mark, G.; Oliver, N.H.S.; Pearson, N. Trace element geochemistry of magnetite and pyrite in Fe oxide (+/−Cu–Au) mineralised systems: Insights into thegeochemistry of ore-forming fluids. *Geochim. Cosmochim. Acta.* **2006**, *70*, 5.
18. Dupuis, C.; Beaudoin, G. Discriminant diagrams for iron oxide trace element fingerprinting of mineral deposit types. *Miner. Depos.* **2011**, *46*, 319–335. https://doi.org/10.1007/s00126-011-0334-y.
19. Angerer, T.; Hagemann, S.G.; Danyushevsky, L. High-grade iron ore at Windarling,Yilgarn Craton: A product of syn-orogenic deformation, hypogene hydrothermal alteration and supergene modification in an Archean BIF-basalt lithostratigraphy. *Miner. Depos.* **2013**, *48*, 697–728.
20. Nadoll, P.; Mauk, J.L.; Hayes, T.S.; Koenig, A.E.; Box, S.E. Geochemistry of magnetite from hydrothermal ore deposits and host rocks of Mesoproterozoic Belt Supergroup, United States. *Econ. Geol.* **2012**, *107*, 1275–1292. https://doi.org/10.2113/econgeo.107.6.1275.
21. Boutroy, E.; Dare, S.A.S.; Beaudoin, G.; Barnes, S.J.; Lightfoot, P.C. Magnetite composition in Ni-Cu-PGE deposits worldwide and its application to mineral exploration. *J. Geochem. Explor.* **2014**, *145*, 64–81.
22. Huang, X.W.; Qi, L.; Meng, Y. Trace element geochemistry of magnetite from the Fe (-Cu) deposits in the Hami region, Eastern Tianshan Orogenic Belt, NW China. *Acta. Geol. Sin.* **2014**, *88*, 176–195.
23. Ciobanu, C.L.; Cook, N.J. Skarn textures and a case study: The Ocna de Fier-Dognecea ore field, Banat, Romania. *Ore Geol. Rev.* **2004**, *24*, 315–370.
24. Monteiro, L.V.S.; Xavier, R.P.; de Carvalho, E.R.; Hitzman, M.W.; Johnson, C.A.; Filho, C.R.D.S.; Torresi, I. Spatial and temporal zoning of hydrothermal alteration and mineralization in the Sossego iron oxide–copper-gold deposit,Carajas Mineral Province,Brazil: Paragenesis and stable isotope constraints. *Miner. Depos.* **2008**, *43*, 129–159. https://doi.org/10.1007/s00126-006-0121-3.
25. Skirrow, R. "Hematite-group" IOCGÂ± U ore systems: Tectonic settings, hydrothermal characteristics, and Cu-Au and U mineralizing processes. In *Exploring for Iron Oxide Copper-Gold Deposits: Canada and Global Analogues*; Corriveau, L., Mumin, H., Eds.; Geological Association of Canada: St. John's, NL, Canada, 2010; Volume 20, pp. 39–58.
26. Nadoll, P.; Angerer, T.; Mauk, J.L.; French, D.; Walshe, J. The chemistry of hydrothermal magnetite: A review. *Ore Geol. Rev.* **2014**, *61*, 1–32. https://doi.org/10.1016/j.oregeorev.2013.12.013.
27. Mukherjee, R.; Venkatesh, A.S. Chemistry of magnetite-apatite from albitite and carbonate hosted Bhukia Gold Deposit, Rajasthan, western India–An IOCG-IOA analogue from Paleoproterozoic Aravalli Supergroup: Evidence from petrographic, LAICPMS and EPMA studies. *Ore Geol. Rev.* **2017**, *91*, 509–529. http://dx.doi.org/10.1016/j.oregeorev.2017.09.005.
28. Dora, M.L.; Upadhyay, D.; Randive, K.R.; Shareef, M.; Baswani, S.R.; Ranjan, S. Trace element geochemistry of magnetite and pyrite and sulfur isotope geochemistry of pyrite and barite from the Thanewasna Cu-(Au) deposit, western Bastar Craton, central India: Implication for ore genesis. *Ore Geol. Rev.* **2020,** *117*, 103262.https://doi.org/10.1016/j.oregeorev.2019.103262.
29. Belousova, E.A.; Griffin, W.L.; O'Reilly, S.Y.; Fisher, N.I. Apatite as an indicator mineral for mineral exploration: Trace-element composition and their relationship to host rock type. *J. Geochem. Explor.* **2002**, *76*, 45–69.
30. Imai, A. Variation of Cl and SO3 contents of micropheno-crystic apatite in intermediate to silicic igneous rocks of Cenozoic Japanese island arcs: Implications for porphyry Cu metallogenesis in the Western Pacific Island arcs. *Res. Geol.* **2004**, *54*, 357–372.
31. FareeduddinKirmani, I.R.; Chander, S. Petrology,geochemistry and fluid inclusion studies of Cu-Au mineralization in paleoproterozoicSalumber-Ghatol belt, Aravalli Supergroup, Rajasthan. *J. Geol. Soc. India* **2012**, *80*, 5–38.
32. Mukherjee, R.; Venkatesh, A.S.; Fareeduddi. Albitite hosted gold-sulfide mineralization: An example from Paleoproterozoic Aravalli supracrustal sequence,Bhukia area, Western India. *Episodes* **2016**, *39*, 590–598. http://dx.doi.org/10.18814/epiiugs/2016/v39i4/103891.
33. Deol, S.; Deb, M.; Large, R.R.; Gilbert, S. LA-ICPMS and EPMA studies of pyrite, arsenopyrite and loellingite from the Bhukia-Jagpura gold deposit, southern Rajasthan, India: Implications for ore genesis and gold remobilization. *Chem. Geol.* **2012,** *326–327*, 72–87.http://dx.doi.org/10.1016/j.chemgeo.2012.07.017.
34. Kumar, M. *Report on Exploration for Gold-Copper Mineralization in Jagpura Area,Banswara District, Rajasthan*; Unpublished Report;Geological Survey of India: Kolkata, India, 2014.
35. Anand, A. *Report on Ore Microscopic, Petrographic and Metamorphic Studies of Prospect Sequence of Bhukia-Jagpura Area,Banswara District, Rajasthan*; Unpublished Report; Geological Survey of India: Kolkata, India, 2016.
36. Skirrow, R.G. Iron oxide copper-gold (IOCG) deposits—A review (part 1): Settings, mineralogy, ore geochemistry and classification. *Ore Geol. Rev.* **2021**, *140*, 104569. https://doi.org/10.1016/j.oregeorev.2021.104569.
37. Gopalan, K.; Macdougall, J.; Roy, A.; Murali, A. Sm-Nd evidence for 3.3 Ga old rocks in Rajasthan, northwestern India. *Precambrian Res.* **1990**, *48*, 287–297. https://doi.org/10.1016/0301-9268(90)90013-G.
38. Roy, A.B.; Kröner, A. Single zircon evaporation ages constraining the growth of the Archaean Aravalli craton, northwestern Indian Shield. *Geol. Mag.***1996**, *133*, 333–342. https://doi.org/10.1017/S0016756800009067.
39. Golani, P.R.; Pandit, M.K.; Sial, A.; Fallick, A.E.; Ferreira, V.P.; Roy, A.B. B-Na rich Paleoproterozoic Aravalli metsediments of evaporitic association, NW India: A new repository of gold mineralization. *Precambrian Res.* **2002**, *116*, 183–198. https://doi.org/10.1016/S0301-9268(02)00020-7.

40. Kaur, P.; Chaudhri, N.; Raczek, I.; Kröner, A.; Hofmann, A.W.; Okrusch, M. Zircon ages of late Palaeoproterozoic (ca. 1.72–1.70 Ga) extension-related granitoids in NE Rajasthan, India: Regional and tectonic significance. *Gondwana Res.* **2011**, *19*, 1040–1053. https://doi.org/10.1016/j.gr.2010.09.009.
41. Fareeduddin; Banerjee, D.M. Aravalli Craton and its Mobile Belts: An Update. *Episodes* **2019**, *43*, 88–108. https://doi.org/10.18814/epiiugs/2020/020005.
42. Roy, A.B.; Sharma, B.L.; Paliwal, B.S.; Chauhan, N.K.; Nagori, D.K.; Golani, P.R.; Bejarniya, B.R.; Bhu, H.; Ali Sabah, M. Lithostratigraphy and tectonic evolution of the Aravalli Supergroup: A proto geosynclinal sequence. In *Rift Basins and Aulacogens*; Casshyap, S.M., Ed.; GyanodayaPrakashan: Naini Tal, India, 1993; pp. 73–90.
43. Pradhan, V.R.; Meert, J.G.; Pandit, M.K.; Kamenov, G.; Gregory, L.C.; Malone, S.J. India's changing place in global Proterozoic reconstructions: A review of geochronologic constraints and Paleomagnetic poles from the Dharwar, Bundelkhand and Marwar cratons. *J. Geodyn.* **2009**, *50*, 224–242. https://doi.org/10.1016/j.jog.2009.11.008.
44. Deb, M.; Sarkar, S.C. Proterozoic tectonic evolution and metallogenesis in the Aravalli Delhi Orogenic belt, northwest India. *Precamb. Res.* **1990**, *46*, 115–137.
45. Singh, S.P. Stratigraphy and sedimentation pattern in the Proterozoic Delhi Supergroup, Northwestern India. *Mem. Geol. Soc. India* **1988**, *7*, 193–206.
46. Bhattacharya, H.N.; Bull, S. Tectono-sedimentary setting of the Paleoproterozoic Zawar Pb–Zn deposits, Rajasthan, India. *Precamb. Res.* **2010**, *177*, 323–338.https://doi.org/10.1016/j.precamres.2010.01.004.
47. Ahmad, T.; Dragusanu, C.; Tanaka, T. Provenance of Proterozoic Basal Aravalli mafic volcanic rocks from Rajasthan, Northwestern India: Nd isotopes evidence for enriched mantle reservoirs. *Precambrian Res.* **2008**, *162*, 150–159. https://doi.org/10.1016/j.precamres.2007.07.011.
48. McKenzie, N.R.; Hughes, N.C.; Myrow, P.M.; Banerjee, D.M.; Deb, M.; Planavsky, N.J. New age constraints for the Proterozoic Aravalli-Delhi successions of India and their implications. *Precambrian Res.* **2013**, *238*, 120–128.https://doi.org/10.1016/j.precamres.2013.10.006.
49. Grover, A.K.; Verma, R.G. Gold mineralization in the Precambrian (Bhukia Area) of southeastern Rajasthan—A new discovery. *J. Geol. Soc. India* **1993**, *42*, 281–288.
50. Chander, S.; Sisodia, C.P. Gold mineralization in the Palaeoproterozoic rocks of Sanjela-Manpur-Dugocha belt,Salumber area, Udaipur district, Rajasthan. *J. Geol. Soc. India* **2003**, *61*, 463–470.
51. Gupta, S.N.; Arora, Y.K.; Mathur, R.K.; Iqbaluddin Prasad, B.; Sahai, T.N.; Sharma, S.B. The Precambrian geology of the Aravalli region, southern Rajasthan and northeastern Gujarat. *Mem. Geol. Surv. India* **1997**, *123*, 262.
52. Sengupta, S. Structures and stratigraphic relations of Aravallis, southeastern Rajasthan. *J. Geol. Soc. India*. **1976**, *4*, 461–470.
53. Sharma, R.S. Patterns of metamorphism in the Precambrian rocks of the Aravalli Mountain Belt. *Mem. Geol. Soc. India* **1988**, *7*, 33–75.
54. Geological Survey of India. *Base Document on Precious Metals and Minerals: Gold, Diamond, PGE and Precious Stones for CGPB Committee–II*; Geological Survey of India: Kolkata, India, 2020, *Unpublished Report*.
55. Deb, M.; Goldfarb, R.J. Gold metallogeny: India and beyond. *Miner. Depos.* **2010**, *46*, 835–836.
56. Deb, M. Some key issues of gold metallogeny in India. *International Workshop in Gold Metallogeny*; Abstract; Delhi University: Delhi, India, 2008; pp. 50–53.
57. Singh, S. *Report on Investigation for Gold and Associated Basemetal Mineralization in Jagpura Block, Banswara District, Rajasthan*; Geological Survey of India: Kolkata, India, 2012, *Unpublished Report*.
58. Kumar, M.; Mohan, L. *Exploration for Gold-Copper Mineralisation in Jagpura Area,Banswara District, Rajasthan*; Geological Survey of India: Kolkata, India, 2016, *Unpublished Report*.
59. Hoefs, J. *Stable Isotope Geochemistry*; Springer: Berlin/Heidelberg, Germany, 2009; p. 288.
60. De Groot, P.A. *Handbook of Stable Isotope Analytical Techniques*; Elsevier: Amsterdam, The Netherlands, 2009; Volume 2, p. 1372.
61. Zhang, Q.L.; Ding, T.P. Analysis of the reference material NBS-123 and the atomic weight of sulfur. *Chinese Sci. Bull.* **1989**, *34*, 1086–1089.
62. Boyle, R.W. *Gold History and Genesis of Deposits*; Van Nostrand-Reinhold Company: New York, NY, USA, 1987; pp. 583–585.
63. Fleet, M.E.; Chryssoulis, S.L.; MacLean, P.J.; Davidson, R.; Weisener, G. Arsenian pyrite from gold deposits: Au and As distribution investigated by SIMS and EP, and color staining and surface oxidation by XPS and LIMS. *Can. Mineral.* **1993**, *31*, 1–17.
64. Bajwah, Z.U.; Seccombe, P.K.; Offler, R. Trace element distribution, Co/Ni ratios and genesis of the Big Cadia iron-copper deposit, New South Wales, Australia. *Miner. Depos.* **1987**, *22*, 292–300.https://doi.org/10.1007/BF00204522.
65. Canil, D.; Grondahl, C.; Lacourse, T.; Pisiak, L.K. Trace elements in magnetitefrom porphyry Cu-Mo-Audeposits in British Columbia, Canada. *Ore Geol. Rev.* **2016**, *72*, 1116–1128.
66. Roedder, E. Fluid Inclusions. Reviews in mineralogy. *Min. Soc. Am.* **1984**, *12*, 644.
67. Brown, P.E.; Lamb, W.M. P-V-T properties of fluids in the system H2O-CO2-NaCl: New graphical presentation and implications for fluid inclusion studies. *Geochim. Cosmochim. Acta.* **1989**, *53*, 1209–1221.https://dx.doi.org/10.1016/0016-7037(89)90057-4.
68. Van den kerkhof, A.M. The System CO_2–CH_4–N_2 in Fluid Inclusions: Theoretical Modelling and Geological Applications. Ph.D. Thesis, Vrije Universiteit Amsterdam, Amsterdam, The Netherland, 1988, p. 206.
69. Shepherd, T.J.; Rankin, A.H.; Alderton, D.H.M. *A Practical Guide to Fluid Inclusion Studies*; Blackie: Glasgow/London, UK, 1985; p. 239.

70. Cook, N.J.; Ciobanu, C.L.; Mao, J. Textural control on gold distribution in As-free pyrite from the Dongping,Huangtuliang and Hougou gold deposits, North China Craton (Hebei Province, China). *Chem. Geol.* **2009**, *264*, 101–121. https://doi.org/10.1016/j.chemgeo.2009.02.020.
71. Zhao, H.X.; Frimmel, H.E.; Jiang, S.Y.; Dai, B.Z. LA-ICP-MS trace element analysis of pyrite from the Xiaoqinling gold district, China: Implications for ore genesis. *Ore Geol. Rev.* **2011**, *43*, 142–153. https://doi.org/10.1016/j.oregeorev.2011.07.006.
72. Liu, W.; Zhang, J.; Sun, J.; Zhou, L.; Liu, A. Low-Ti iron oxide deposits in the Emeishan large igneous province related to low-Ti basalts and gabbroic intrusions. *Ore Geol. Rev.* **2015**, *65*, 180–197.
73. Zhou, M.F.; Chen, W.T.; Wang, C.Y.; Prevec, S.A.; Liu, P.P.; Howarth, G.H. Two stages of immiscible liquid separation in the formation of Panzhihua-type Fe–Ti–Voxide deposits, SW China. *Geosci. Front.* **2013**, *4*, 481–502.
74. Ray, G.; Webster, I. Geology and chemistry of the low Ti magnetite-bearing Heff Cu-Au skarn and its associated plutonic rocks,Heffley Lake, south-central British Columbia. *Explor. Min. Geol.* **2007**, *16*, 159–186. https://doi.org/10.2113/gsemg.16.3-4.159.
75. Blanc, P.P. Distinction between magmatic and hydrothermal signature in apatite from north Portugal Cathodoluminescence,SEM and electron microscopic study. *Bull. Soc. Geol. France.* **1994**, *165*, 329–339.
76. Gehrig, M.; Lentz, H.; Franck, E.U. Thermodynamic properties of water–carbon dioxide–sodium chloride mixtures at high temperatures and pressures. In *High Pressure Science and Technology*; Timmerhaus, K.D.; Barber, M.S., Eds.; Physical Properties and Material Synthesis; Springer: Berlin/Heidelberg, Germany, 1979; Volume 1, pp. 539–542.
77. Vityk, M.O.; Bodnar, R.J.; Schmidt, C.S. Fluid inclusions as tectonothermobarometers: Relation between pressure–temperature history and re-equilibration morphology during crustal thickening. *Geology* **1994**, *22*, 731–734.
78. Wilkinson, J.J. Fluid inclusions in hydrothermal ore deposits. *Lithos* **2001**, *55*, 229–272.https://doi.org/10.1016/S0024-4937(00)00047-5.
79. Kesler, S.E.; Haynes, P.S.; Creech, M.Z.; Gorman, J.A. Application of fluid inclusion and rock gas analysis in mineral exploration. *J. Geochem. Explor.* **1986**, *25*, 201–215. https://doi.org/10.1016/0375-6742(86)90014-2.
80. Kesler, S.E. Ore forming fluids. *Elements* **2005**, *1*, 13–18. https://doi.org/10.2113/gselements.1.1.13.
81. Seal, R.R. Sulfur Isotope Geochemistry of Sulfide Minerals. *Rev. Mineral. Geochem.* **2006**, *61*, 633–677.
82. Holser, W.T. Catastrophic chemical events in the history of the ocean. *Nature* **1977**, *267*, 402–408.
83. Zhao, L.; Chen, H.; Zhang, L.; Xiaoping, X.; Zhang, W.; Li, D.; Lu, W.; Liang, P.; Li, R.; Yang, J.; et al. Geology and ore genesis of the late PaleozoicHeijianshan Fe oxide–Cu (–Au) deposit in the Eastern Tianshan, NW China. *Ore Geol. Rev.* **2017**, *91*, 110–132.
84. Pal, D.C.; Barton, M.D.; Sarangi, A.K. Deciphering a multistage history affecting U-Cu (–Fe) mineralization in the Singhbhum Shear Zone, eastern India using pyrite textures and compositions in the Turamdih U–Cu (–Fe) deposit. *Miner. Depos.* **2009**, *44*, 61–80. https://doi.org/10.1007/s00126-007-0165-z.
85. Neilsen, H. Sulfur isotopes. In *Lectures in Isotope Geology*; Jager, E.; Hunziher, J.E., Eds.; Springer: Berlin/Heidelberg, Germany, 1979; pp. 283–312.
86. Ohmoto, H.; Goldhaber, M.B. Sulfur and carbon isotopes. In *Geochemistry of Hydrothermal Ore Deposits*; Barnes, H.L., Ed.;John Wiley and Sons: Hoboken, NJ, USA,1997; pp. 517–611.
87. Eldridge, C.S.; Compston, W.; Williams, I.S.; Harris, J.W.; Bristow, J.W. Isotope evidence for the involvement of recycled sediments in the diamond formation. *Nature***1991,** *353*, 649–653.
88. Bastrakov, E.N.; Skirrow, R.G.; Davidson, G.J. Fluid Evolution and origins of iron oxide Cu-Au prospects in the Olympic Dam District, Gawler Craton, South Australia. *Econ. Geol.* **2007**, *102*, 1415–1440. https://doi.org/0361-0128/07/3709/1415-26.
89. De Haller, A.; Fontboté, L. The Raul-Condestable iron oxide copper-gold deposit, central coast of Peru: Ore and related hydrothermal alteration, sulfur isotopes, and thermodynamic constraints: *Econ. Geol.* **2009**, *104*, 365–384.
90. Chen, H.Y. External sulfur in IOCG mineralization: Implications on the definition and classification of the IOCG clan. *Ore Geol. Rev.* **2013**, *51*, 74–78.
91. Ault, K.M.; Williams-Jones, A.E. Sulfur and lead isotope study of the EL Mochito Zn-Pb-Ag deposit. *Econ. Geol.* **2004**, *99*, 1223–1231. https://doi.org/10.2113/gsecongeo.99.6.1223.
92. Hutchison, W.; Finch, A.A.; Boyce, A.J. The sulfur isotope evolution of magmatic-hydrothermal fluids: Insights into ore-forming processes. *Geochim. Cosmochim. Acta.* **2020**, *288*, 176–198. https://doi.org/10.1016/j.gca.2020.07.042.
93. Rollinson, H.R. *Using Geochemical Data: Evaluation, Presentation, Interpretation*; Longman: London, UK, 1993.
94. Hitzman, M.W. Iron oxide-Cu-Au deposits: What, where, when, and why. In *Hydrothermal Iron Oxide Copper-Gold and Related Deposits; A Global Perspective*; Porter, T.M., Ed.; Australian Mineral Foundation: Adelaide, Australia, 2000; Volume 1, pp. 9–25.
95. Williams, P.J.; Skirrow, R.G. Overview of iron oxide–copper–gold deposits in the Curnamona Province and Cloncurry District (Eastern Mount Isa Block). In *A Global Perspective*; Porter, T.M., Ed.; PGC Publishing: Brisbane, Australia, 2000; Volume 1, pp. 105–122.
96. Williams, P.J.; Barton, M.D.; Johnson, D.A.; Fontbote, L.; De Haller, A.; Mark, G.; Oliver, N.H.S.; Marschik, R. Iron oxide copper-gold deposits: Geology, space-time distribution and possible modes of origin. *Econ. Geol.* **2005**, *100*, 371–405.
97. Davidson, G.J.; Hamish, P.; Sebastien, M.; Ron, F.B.Characteristics and origin of the Oak Dam East breccia-hosted, iron oxide Cu–U–(Au) deposit: Olympic Dam region,Gawler Craton, South Australia. *Econ. Geol.* **2007**, *102*, 1471–1498.
98. Barton, M.D. Iron oxide (-Cu-Au-REE-P-Ag-U-Co) systems. In *Treatise on Geochemistry*, 2nd ed.; Elsevier Inc.: Amsterdam, The Netherlands, 2014; pp. 515–541.